# Effects of Polymer Concentration and Molecular Weight on the Dynamics of Visco-Elasto-Capillary Breakup

by

Matthieu Verani

Submitted to the Department of Aeronautics and Astronautics
in partial fulfillment of the requirements for the degree of

Master of Science in Aeronautics and Astronautics

at the

MASSACHUSETTS INSTITUTE OF TECHNOLOGY

January 2004



Author .....
Department of Aeronautics and Astronautics
January 29, 2004

Certified by .....
Gareth McKinley
Professor of Mechanical Engineering
Thesis Supervisor

Accepted by .....
Edward M. Greitzer
H.N. Slater Professor of Aeronautics and Astronautics
Chair, Committee on Graduate Students

# Effects of Polymer Concentration and Molecular Weight on the Dynamics of Visco-Elasto-Capillary Breakup

by

Matthieu Verani

Submitted to the Department of Aeronautics and Astronautics
on January 29, 2004, in partial fulfillment of the
requirements for the degree of
Master of Science in Aeronautics and Astronautics

## Abstract

Capillary-break-up measurements of viscoelastic polymer solutions are performed using a Capillary Breakup Extensional Rheometer (CABER). The device consists of two coaxial plates which are used to form and hold a liquid bridge of the test fluid. An axial step strain is applied to the fluid by raising the top plate and the elongated fluid thread then evolves towards breakup under the combined action of viscous, elastic and capillary forces. The test fluids used in the present study are a series of diluted polystyrene Boger fluids ('PS025' and its dilutions) and a new polystyrene Boger fluid (labelled 'MV1') comprising of a lower molecular weight solute. This fluid is less susceptible to gravity, and allows us to observe the coil-stretch transition of high molecular weight polymers. The persistent dependence of the measured relaxation time on concentration, even in the dilute regime predicted from theory, is demonstrated both experimentally and numerically. Indeed, numerical simulations of the evolution of the stress contributions and of the radius using a single mode FENE-P model based on the one-dimensional analysis of Entov and Hinch for transient extensional flows are compared to the experimental observations of the radius of the liquid filament. Below a critical dilution, the stress in the necking thread is carried solely by the solvent with no appreciable contribution from the polymer chains, and the dynamics of the necking process change appreciably. A sensitive force transducer is also added to the CABER. This allows us to measure the initial tensile stress resulting from the axial step strain. Existing one dimensioned models for analyzing capillary breakup measurements have assumed this to be identically zero. However recent similarity solutions for viscoelastic models have shown that in fact the force is not zero but monotonically decays towards zero at the same necking rate as the filament radius. We present the first experimental measurements of this small but finite ($\approx \mathcal{O}(10^{-4}\ N)$) tensile force and show that indeed it decays with similar dynamics to the measured radius.

Thesis Supervisor: Gareth McKinley
Title: Professor of Mechanical Engineering

# Acknowledgments

I would like to thank my advisor, Gareth McKinley, for the opportunity he gave me to do research with his group and for his numerous and supportive advices. I am thankful I was able to work in such a stimulating environment.

I want to thank my successive desk mates (Anna, Trevor and Lucy) for being understanding about my English and for standing my sense of humor (?). I also thank my lab mates in the Hatsopoulos Microfluids Laboratory, especially José for his assistance and his insightful ideas, and Benjamin who assisted me when I was "handicapped". In connection with that, my insurance company sends its appreciations to the lab's soccer team...

# Contents

# List of Figures

# List of Tables

# Nomenclature

### Abbreviations

| | |
|---|---|
| Bo | Bond Number |
| Ca | Capillary Number |
| CABER | Capillary Breakup Extensional Rheometer |
| De | Deborah Number |
| EC | Elasto-Capillary |
| FE | Fully Extended |
| FENE | Finitely Extensible Nonlinear Elastic |
| FENE-P | Finitely Extensible Nonlinear Elastic by Peterlin |
| Oh | Ohnesorge Number |
| VC | Visco-Capillary |

### Symbols

| | |
|---|---|
| $\underline{\underline{A}}$ | Deformation tensor |
| $c$ | Concentration |
| $c^*$ | Coil Overlap concentration |
| $f_i$ | FENE factor |
| $G_i$ | Elastic Moduli |
| $h^*$ | Hydrodynamic Interaction parameter |
| $M_w$ | Molecular Weight |
| $R$ | Radius of the filament of liquid |

### Greek Symbols

| | |
|---|---|
| $\dot{\epsilon}$ | Strain-rate |
| $[\eta]$ | Intrinsic Viscosity |
| $\eta_0$ | Total Viscosity |
| $\eta_s$ | Solvent Viscosity |
| $\underline{\underline{\dot{\gamma}}}$ | Strain-rate tensor |
| $\lambda$ | Relaxation Time |
| $\nu$ | Excluded Volume parameter |
| $\sigma$ | Surface Tension |
| $\zeta$ | Riemann Zeta function |

# Chapter 1

# Introduction

This study is in keeping with a general study of polymer solutions by extensional rheometry. The Capillary Breakup Extensional Rheometer (CABER) described in chapter 3 is a device which has already been used to determine the relaxation times of polymer solutions, but only in order to scale them with the molecular weight of the polymer chain $M_w$. It is discussed for example by Anna et al. ([AM01] and [AMN$^+$01]). Nevertheless, such a study has never been done to scale the relaxation times with the concentration of polymer in very dilute solutions. The following study takes an interest in very dilute Biger fluids and the evolution of the relaxation times with the concentration. Both experimental and numerical methods are used to determine the relaxation times.

Concerning a numerical simulation of the behavior of a visco-elastic fluid during a CABER experiment, several papers such as [EH97] propose a set of equations to explain the phenomena we observe. These equations are implemented in a Matlab code in chapter 4. The goal is to explain the behavior of the visco-elastic fluids experimentally observed in chapter 3. Yet there is a parameter of the code that we need to guess: the initial axial stress in the filament $A^0_{zz}$ is unknown. First, it will be stated as equal to 1, as if there were no deformation. This value is obviously not satisfying and Anna proposed a formula for $A^0_{zz}$ in [AM01]. It is also possible to measure the initial stress and it is done in chapter 6. This parameter has a great impact in the shape of the numerical simulation of visco-elastic fluids.

Finally, the effects of gravity are often neglected when dealing with such small volume of visco-elastic fluids as in CABER experiments. We can nonetheless observe a drainage during the necking of the liquid filament. Since we do not know exactly the importance of the gravity in our experiments, it is interesting to make a fluid less susceptible to gravity and too run experiments with it.

# Chapter 2

# Literature review

## 2.1 Strain-rate tensor in a liquid filament

A fluid configuration of interest is a liquid filament formed by loading a sample between two horizontal plates and applying a step strain (as shown in figure 2-1). This will be the reference configuration for the Caber (Capillary Breakup Extensional Rheometer) experiments (section 3.1).

Figure 2-1: *Liquid filament bridge is formed between two plates after application of a step strain.*

The liquids then selects the dynamics such that the capillary, viscous and elastic stresses balance each other [MT00]. Bazilevsky et al. [BER01] show that the pressure in the droplets at the end of the filament is lower than the pressure within the filament.

As a result the fluid flows to the droplets. This necking is geometrically modeled by a cylinder of fluid connected to two horizontal fixed end plates (figure 2-2).

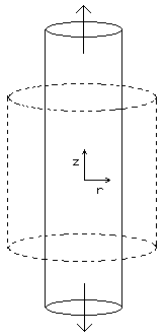


Figure 2-2: *Model of a liquid filament bridge during necking process as a regular cylinder.*

For a fixed volume of liquid, two equal droplets take up less surface area than a cylinder. Therefore, according to the Rayleigh instability, a cylinder is not a stable configuration and leads naturally to the thinning of the filament as observed experimentally [Egg97]. This thinning is then modeled as steady simple elongational flow corresponding to the following equations [Ren94]:

$$\nu_r = -\frac{1}{2}\dot{\epsilon}r, \tag{2.1}$$

$$\nu_\theta = 0, \tag{2.2}$$

$$\nu_z = \dot{\epsilon}z, \tag{2.3}$$

where $z$ is along the length of the filament, $r$ is the radius and $\dot{\epsilon}$ is the elongational strain rate. Differentiating these expressions gives the velocity gradient:

$$\underline{\nabla}\,\underline{\nu} = \begin{pmatrix} \frac{\partial \nu_r}{\partial r} & 0 & 0 \\ 0 & \frac{1}{r}\frac{\partial \nu_\theta}{\partial \theta} + \frac{\nu_r}{r} & 0 \\ 0 & 0 & \frac{\partial \nu_z}{\partial z} \end{pmatrix}$$

The strain rate tensor is:

$$\underline{\underline{\dot{\gamma}}} = \underline{\nabla}\,\underline{\nu} + (\underline{\nabla}\,\underline{\nu})^t = \begin{pmatrix} -\dot{\epsilon} & 0 & 0 \\ 0 & -\dot{\epsilon} & 0 \\ 0 & 0 & 2\dot{\epsilon} \end{pmatrix}$$

where $\dot{\epsilon}$ is the elongational strain rate defined by the radius of the filament at mid-height $R$ by [BAH87]:

$$\dot{\epsilon} = -\frac{2}{R}\frac{dR}{dt}, \tag{2.4}$$

because of the radial boundary condition $\nu_r(r = R) = \frac{dR}{dt}$, where $\nu_r$ is given by the equation 2.1. This kind of flow is discussed in numerous papers including those of Doyle et al. [DSMS98], Entov [Ent99], Rasmussen and Hassager [RH99], and Bach et al. [BARH03].

## 2.2 Newtonian fluid

For a newtonian fluid, the total stress in the radial direction ($\pi_{rr}$) and axial direction ($\pi_{zz}$) is given by [LM94]:

$$\pi_{rr} = -p_0 + \eta_s\dot{\gamma_{rr}} = -\frac{\sigma}{R}, \tag{2.5}$$

$$\pi_{zz} = -p_0 + \eta_s\dot{\gamma_{zz}} = 0. \tag{2.6}$$

$p_0$ is the atmospheric pressure, $\eta_s$ is the viscosity and $\sigma$ is the surface tension. The axial stress is equal to zero because each end of the filament is attached to the relatively quasi-static large droplets. The elongational stress is then:

$$\pi_E = \pi_{zz} - \pi_{rr} = 3\eta\dot{\epsilon} = \frac{\sigma}{R}. \tag{2.7}$$

Integrating this equation with equation 2.4 yields:

$$R(t) = R_0 - \frac{\sigma t}{6\eta_s}, \tag{2.8}$$

where $R_0$ is the radius at initial time (corresponding to the end of the step strain) [KS99]. The decrease of the radius for a newtonian fluid is then linear in time.

In this model, the stress along the z-axia is assumed euqal to zero. This assumption is not exact and so this theory does not correlate well with the experimental data. A correction factor $X$ has to be added as discussed in [MT00]. The equation 2.8 becomes:

$$R(t) = R_0 - \frac{(2X-1)\sigma t}{6\eta_s}. \tag{2.9}$$

This numerical factor $X$ is discussed in various papers including those of Eggers [Egg93] & [Egg97], Papageorgiou [Pap95] and Renardy [Ren95]. The value used for viscous Newtonian fluids is $X = 0.7127$ [Pap95].

## 2.3 Viscoelastic fluid: Kinetic theories

Some usual references on bead-spring kinetic theories for dilute polymer solutions include articles and books by Bird et al. [BAHC87], Larson [Lar88], Rouse [Rou53] and Zimm [Zim56]. A viscoelastic fluid is a non-newtonian fluid with viscous and elastic properties. Experimental and theoretical achievements in rheology allowed a hierarchical description of the fluid microstructure that can be systematically reduced in dimensionality (coarse grained)[MS02]. A summary of this process is given by the figure 2-3.

The more 'coarse-grained' level consists in modeling the macromolecules of a polymer solution as Finitely Extensible Non-linear Elastic (FENE) dumbbells [dG97] & [BAHC87]. The dumbbells are two beads attached by a spring which is linear for small displacements. The FENE model is a multi-mode constitutive model existing under several variants. As described in [Keu97], the classic approximation by Peterlin (FENE-P model) is the one which is used most commonly to describe viscoelastic fluids: it consists in pre-averaging the non-linear spring law. This model is described in further detail in section 4.1. In the following sections are given the equations of two simpler models which will be used in the study: the Kuhn Chain model and the Zimm theory.

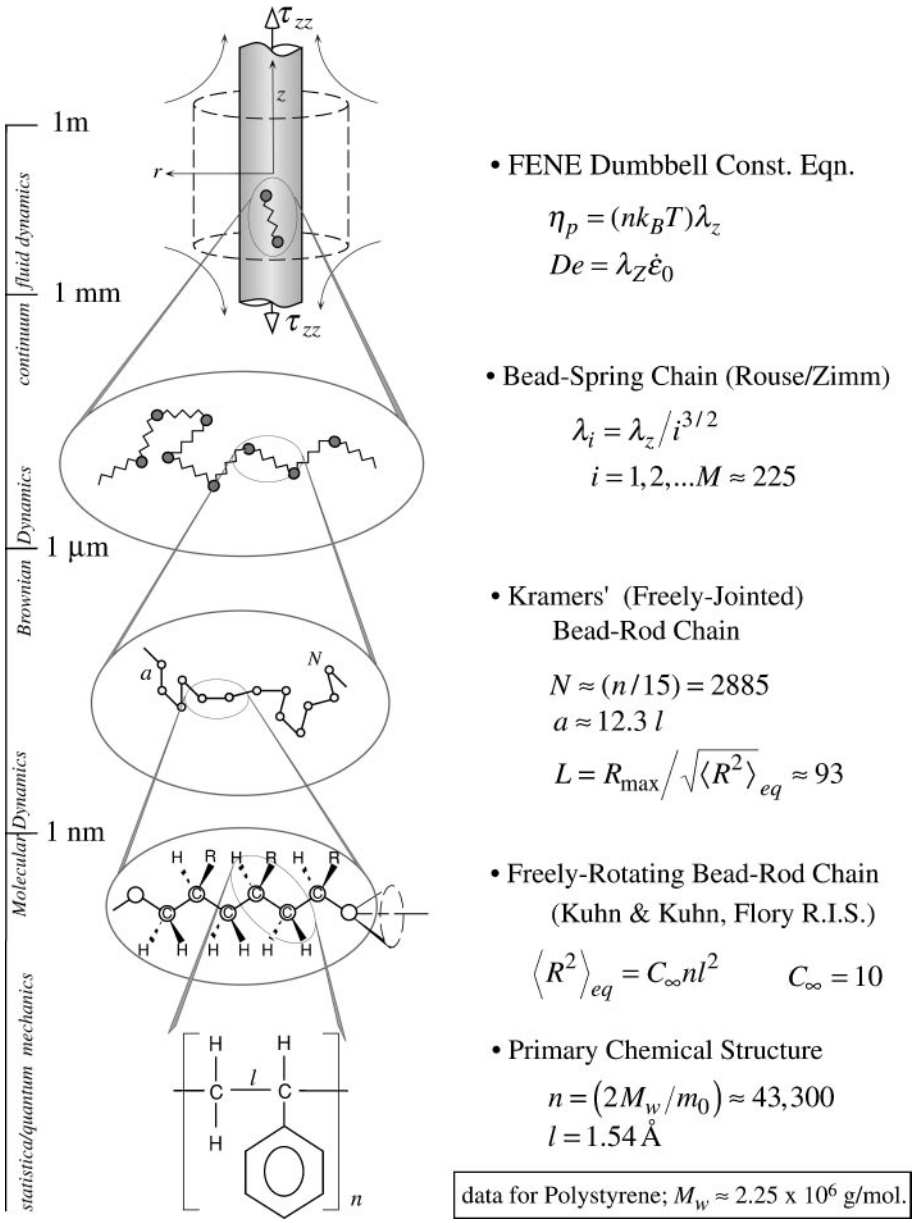


Figure 2-3: *Coarse graining in the hierarchy of microstructural modeling for dilute polymer solutions, extracted from [MS02].*

### 2.3.1 Kuhn Chain

The simplest model replaces the polymer chain by a freely-rotating bead-rod chain: this is the Kuhn chain. This simple model allows to calculate approximations for some of the parameters of the polymer solution.

#### Relaxation time

One can convert molecular information from a real hydrocarbon macromolecule into the parameters describing a Kuhn chain of statistically equivalent freely-rotating rigid rods. Within this framework, a simple expression for the longest relaxation time is [HLL03]:

$$\lambda_{IV} = \frac{1}{\zeta(3\nu)}.\frac{[\eta]\eta_s M_w}{N_A k_B T}, \tag{2.10}$$

where $\nu$ is the excluded volume parameter from the Zimm theory, $\zeta$ is the Riemann zeta function $\zeta(3\nu) = \sum_{i=1}^{\infty} 1/i^{3\nu}$and $[\eta]$ is the intrinsic viscosity. The intrinsic viscosity is a parameter defined as a limit value when the concentration goes to zero: $[\eta] = \lim_{c\to 0} \frac{\eta_s - \eta_o}{c\eta_s}$ [BAHC87]. For the empirical Mark-Houwink-Sakurada equation:

$$[\eta] = K.M_w^{3\nu-1}, \tag{2.11}$$

where $K$ is a scale parameter. The value of the excluded volume exponent for SM Boger fluids has been found to be $\nu = 0.53 \pm 0.015$ [AMN$^+$01]. Solomon and Muller ([SM96a] and [SM96b]) determined the following numerical values for fluids similar to the test fluids: $[\eta] = 4.2 \times 10^{-5} M_w^{0.59} L/g$ with $M_w$ expressed in $g/mol$. Thus, the equation 2.10 provides theoretical values for the longest relaxation times, referred as $\lambda_{IV}$ in what follows.

#### Other physical parameters

The diluteness of the fluid is determined by examining the coil overlap concentration $c^*$:

$$c^* = \frac{M_w}{4/3\pi R_g^3 N_A}, \tag{2.12}$$

where $R_g$ is the radius of gyration [Gra80]. At this concentration $c^*$, the polymer chains do not overlap when at rest. If $c < c^*$, the solution is considered as diluted.

Consequently, from the Kuhn chain model, one can deduce the expression of the coil overlap concentration:

$$c^* = \frac{3}{4\pi N_A}\left(\frac{m_o}{jC_\infty}\right)^{3/2}\frac{1}{l^3}\frac{1}{M_w^{1/2}}, \tag{2.13}$$

where $C_\infty = 10$ is the characteristic ratio of chain, $m_o$ is the mass of the monomeric repeat unit, $j = 2$ is the number of carbon-carbon bonds obtained from each monomer and $l = 1.54\mathring{A}$ is the carbon-carbon bond length.

The finite extensibility parameter $L^2$ is defined as a ratio of the maximum length of the chain to a characteristic length. For dilute solutions and by conventional definition, the characteristic length used is one third of the mean square size of the chain $\langle R^2\rangle/3$. Then, the finite extensibility parameter is given by the equation 2.14:

$$L^2 = 3\left(\frac{j\times 0.816^2}{m_0 C_\infty}\right)^{2(1-\nu)} M_w^{2(1-\nu)}. \tag{2.14}$$

The geometric factor $\sin\left(\tan^{-1}\sqrt{2}\right) = 0.816$ corresponds to a tetrahedrally-bonded carbon-carbon bond angle.

From the Einstein relation for viscosity of a dilute suspension, the total viscosity $\eta_0$ can be expressed as the following function of the solvent viscosity $\eta_s$ and the volume fraction $\phi$:

$$\eta_0 = \eta_s\left[1 + \frac{5}{2}\phi + 0(\phi^2)\right], \tag{2.15}$$

$$\eta_0 = \eta_s(1 + const.\times c). \tag{2.16}$$

$c$ is the concentration and the constant term is equal to $[\eta] + 0(c)$. For a dilute solution, the Taylor-series expansion yields the following expression:

$$\eta_0 = \eta_s(1 + c[\eta] + k''[\eta]^2c^2 + ...), \tag{2.17}$$

where $k''$ is the Huggins constant and $[\eta]$ is the intrinsic viscosity defined in equation 2.11. For dilute solutions where $[\eta]c << 1$, the expression of the total viscosity will be calculated from the simplified equation 2.18:

$$\eta_0 = \eta_s(1 + c[\eta]). \tag{2.18}$$

### 2.3.2 Zimm model and sinusoidal linear viscoelastic response

A more 'coarse-grained' level consists in modeling the polymer chain by a Spring-Bead chain: this is the Rouse theory. Adding hydrodynamic interactions leads to the Zimm theory. Within this framework, the relaxation time of the $i^{th}$ is expressed as a function of the longest relaxation time $\lambda_z$ according to the equation 2.19:

$$\lambda_i = \frac{\lambda_z}{i^{2+\sigma}}, \tag{2.19}$$

where $\sigma \approx -1.4 \times (h^*)^{0.78}$ and $h^*$ is the hydrodynamic interaction parameter, equal to 0.25 for a theta solvent [Lar88].

In the experimental section of this work we use a time-sinusoidal signal applied on a sample of fluid in the linear region of response. The response of the sample is then measured and allows to calculate a relaxation time [Tan99] as we will see later (section 3.3.1). Let considerate a sinusoidal shear strain as input signal:

$$\gamma = \hat{\gamma} \exp(i\omega t). \tag{2.20}$$

The shear stress response is:

$$\tau = \hat{\sigma} \exp(i\omega t). \tag{2.21}$$

Substituting in the form of the viscoelasticity relation for compressible materials given by Pipkin [Pip86] yields:

$$\hat{\sigma} e^{i\omega t} = i\omega\hat{\gamma} \int_{-\infty}^{t} G(t - t') e^{i\omega t'} dt'. \tag{2.22}$$

The complex modulus $G^*$ defined as $\hat{\sigma}/\hat{\gamma}$ is then given by:

$$G^* = i\omega \int_0^\infty G(s)e^{-i\omega s}ds = G' + iG'', \tag{2.23}$$

where $G'(\omega)$ is the storage modulus and $G''(\omega)$ is the loss modulus. We can also define the complex viscosity $\eta^* = \hat{\sigma}/\hat{\dot{\gamma}}$ by:

$$\eta^* = \eta' - i\eta'' = \frac{G^*}{i\omega} = \frac{G''}{\omega} - i\frac{G'}{\omega}. \tag{2.24}$$

$\eta'$ is the dynamic viscosity and it is equal to the steady-flow Newtonian viscosity for a Newtonian fluid. As $\omega \to 0$, the zero-shear rate viscosity is:

$$\eta_0 = \int_0^\infty G(s)ds. \tag{2.25}$$

For the Rouse-Zimm model, the expressions of the storage modulus, the loss modulus and the zero-shear rate viscosity are respectively given by the two following equations:

$$G' = \eta''\omega = \frac{cN_AkT}{M_w}\sum_{i=1}^{N_m}\frac{(\lambda_z\omega)^2}{i^{2(2+\sigma)} + (\lambda_z\omega)^2}, \tag{2.26}$$

$$G'' = \eta'\omega = \eta_s\omega + \frac{cN_AkT}{M_w}\sum_{i=1}^{N_m}\frac{\lambda_z\omega i^{2+\sigma}}{i^{2(2+\sigma)} + (\lambda_z\omega)^2}, \tag{2.27}$$

$$\eta_0 = \eta_s + \frac{cN_AkT}{M_w}\lambda_z\sum_{i=1}^{N_m}\frac{1}{i^{2+\sigma}}, \tag{2.28}$$

with $N_m$ the number of modes.

## 2.4 Non-dimensional numbers

Several dimensionless numbers can characterize the behavior of non-newtonian fluids in free surface flows. The numbers introduced here will be used extensively in the next chapters.

- *Ohnesorge number*: it evaluates the importance of viscous effects over inertial effects in free surface flows. It is defined by:

$$Oh = \frac{\eta_o}{\sqrt{\rho\sigma R}}, \tag{2.29}$$

where $\eta_0$, $\rho$, $\sigma$ and $R$ are respectively the zero-shear viscosity of the fluid, its density, its surface tension and the radius of the liquid filament at mid-height in the case of a Caber experiment (section 3.1). It can also be seen as a Reynolds number

$$Oh^{-2} = \frac{\rho v R}{\eta_o}, \tag{2.30}$$

where the velocity is $v = \sigma/\eta_o$. This velocity corresponds to the speed of the linear decrease of the liquid diameter of a Newtonian fluid as given by the equation 2.8.

- *Deborah number* [Rei69]: it is the dimensionless deformation rate computed as the ratio of the relaxation time of the fluid by the characteristic time of the experiment. Considering the time it would take for the filament to break if there were only inertial forces as the characteristic time, the definition of the Deborah number is

$$De = \frac{\lambda}{\sqrt{\rho R^3/\sigma}}. \tag{2.31}$$

Hence, the ratio of these two numbers leads to an 'Elastocapillary number' which gives the relative effects of elastic forces over viscous forces:

$$\frac{De}{Oh} = \frac{\lambda\sigma}{\eta_o R}. \tag{2.32}$$

- *Bond number*: this dimensionless number describes the competition between gravity, which causes the filament to sag and drain, and surface tension, which acts to maintain the cylindrical shape of the filament. It is defined by the equation 2.33:

$$Bo = \frac{\rho g R^2(t)}{\sigma}, \tag{2.33}$$

where $R$ is the mid-height radius of this filament. This number is a measure of the axial asymmetry of the initial static fluid column about its mid-plane.

- *Capillary number*: it gives the relative effects of viscosity versus surface tension and is defined by equation 2.34.

$$Ca = \frac{\eta_0 U}{\sigma}, \tag{2.34}$$

where $U$ is the imposed velocity. It is then the ratio of $\frac{U}{v}$, where $v = \sigma/\eta_0$ is the velocity defined for the Ohnesorge number. In the following study, a characteristic velocity is $U = \dot{\epsilon}R$ where $\dot{\epsilon}$ is the strain rate.

# Chapter 3

# Effects of concentration

## 3.1 Capillary Breakup Extensional Rheometer

### 3.1.1 Apparatus

The experiments are run using the Capillary Breakup Extensional Rheometer (CABER) made by the Cambridge Polymer Group (www.campoly.com). The instrument characterizes the flow of test liquids in extension. There are two plates in contact with the liquid. They are both $6mm$ in diameter ($2R_0 = 6mm$). At the beginning of an experiment, the gap between the plates is set to be $3mm$, corresponding to a sample of fluid of about $90\mu L$. Then, the bottom plate is held stationary and the top plate moves vertically, applying a step strain to the fluid and stretching it to a final height of $13mm$. The applied strain is at a rate as close as possible to a step with the current setup. This instrument can be seen on figure 3-1.

A laser micrometer measures the radius of the liquid filament over time as it breaks under capillary force (seen on figure 3-2). It has an accuracy of $5 - 10\mu m$ and a resolution of $20\mu m$. The experimental setup is controlled using the CABER software version 3, written in LabVIEW. The data acquisition is done through a National Instrument 1200 DAQ card.

The layout of the experiment setup is presented in figure 3-3 [Par03]. The data from the micrometer travels through the Caber control box and the DAQ card, while

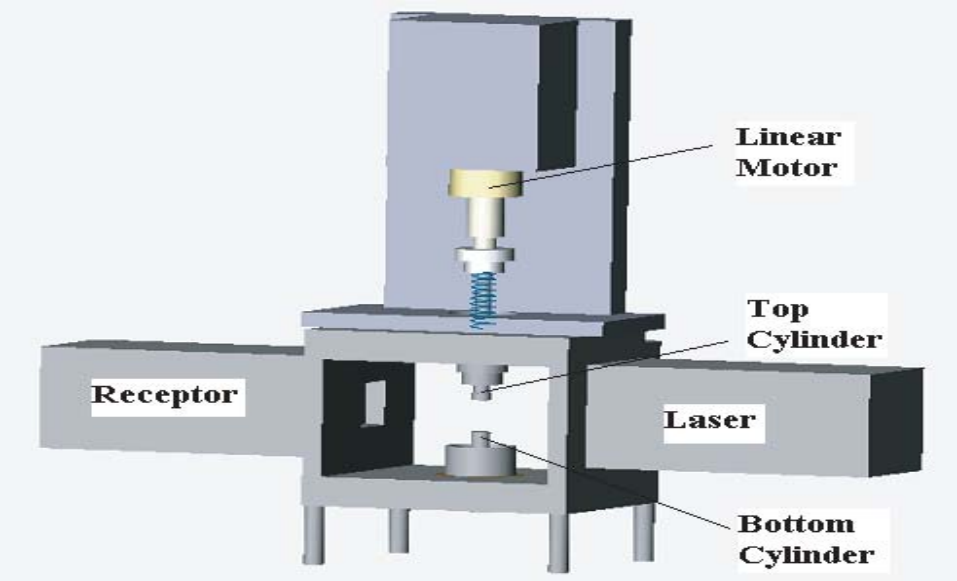


Figure 3-1: *Solidworks drawing of the Caber.*

the data from the linear motor reaches the computer by going trough the motor control box.

### 3.1.2 Running Caber

Running the Caber program first leads to the checking of the correct voltage for the laser micrometer. Then, the motor takes several minutes to calibrate to the given geometry and asks for the desired initial gap. For all the experiments, an initial gap of $L_0 = 3mm$ is used. The test performed is triggered test and you have to choose the duration of the experiment and the sample rate. The user can now choose the strike time, which is the length of time the linear motor takes to raise the top cylinder. To perform a step strain experiment, $50ms$ (the shortest duration allowed by the motor) is inputted. The top cylinder then lowers, allowing operator to load about $90\mu L$ of sample, as shown on figure 3-4. Finally, the top cylinder raises to the final height. The whole process is explained in further detail in [Par03].

The video images of the experiments are recorded using a Cohu camera, model MS12. The experiments are lit from the back using an electroluminescent light sheet.

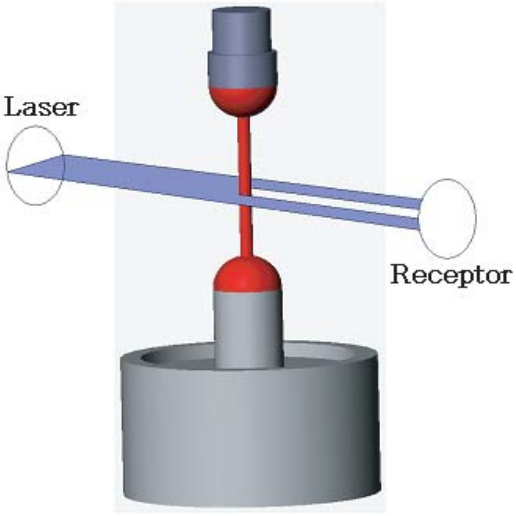


Figure 3-2: *A laser micrometer measures the thickness of the filament.*

## 3.2 Summary of fluids

The test fluids are Boger fluids consisting of high molecular weight polystyrene ($M_w = 1.877 \times 10^6 g/mol$) and styrene oil. A Boger fluid is a dilute solution composed of low concentrations of high molecular weight polymer dissolved in highly viscous Newtonian liquid. The material properties of the reference test fluid called PS025 are discussed more in depth in [Ann00]. The solvent used for the test fluids is oligomeric styrene (Piccolastic A5 Resin) from Hercules. At $25^oC$, the material has a density of $1026 kg/m^3$ and a surface tension of $0.0378 N/m$ measured with a Kruss Digital Tensiometer K10ST [Ten95]. To form PS025, $0.025 wt.\%$ of polystyrene is dissolved in the styrene oil. The other test fluids are dilutions of PS025 in order to obtain concentrations as weak as $0.000025 wt.\%$. For the test fluids, the ratio of the weight concentration over the coil overlap concentration $c^*$ (from equation 2.13 with $C_\infty = 10$, $j = 2$, $m_o = 104\ g/mol$ and $l = 1.54\mathring{A}$) is given on table 3.1. For our fluid, $c^* = 9.4 \times 10^{-4} g/cm^3 = 0.091 wt.\%$.

All of the ratios are far less than 1, indicating that the fluids are dilute.

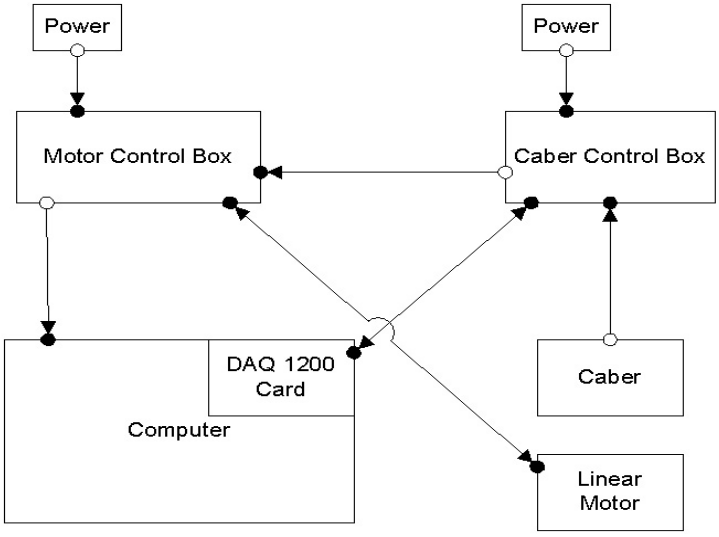


Figure 3-3: *Diagram of the Caber experiment setup.*

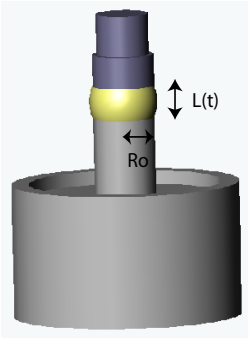


Figure 3-4: *Cylinders after a fluid sample has been loaded.*

## 3.3 Summary of experiments

### 3.3.1 Characterization of the fluid by shear rheology

AR 1000 by TA Instruments is a controlled stress rheometer [Rhe96]. It is used to measure the shear viscosity and the relaxation time of the seven test fluids obtained by successive dilutions of PS025 and exposed in table 3.1. All of the tests are run using cone fixtures with the tip truncated (figure 3-5). The properties of the cone used in the following experiments are gathered in table 3.2.

| **Fluid** | PS025 | PS008 | PS0025 | PS0008 | PS00025 | PS00008 | PS000025 |
|---|---|---|---|---|---|---|---|
| $c/c^*$ | 0.273 | 0.0873 | 0.0273 | 0.00873 | 0.00273 | 0.000873 | 0.000273 |

Table 3.1: *Ratio of the weight concentration and the coil overlap concentration $c^*$ for the test fluids.*

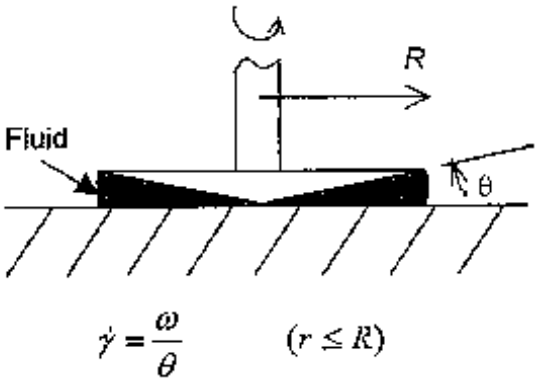


Figure 3-5: *Cone and plate rheometer. The shear rate $\dot{\gamma}$ is constant throughout the fluid (extracted from [Par03]).*

**Steady shear flow: shear viscosity**

A steady flow experiment is chosen with a specified range of stress. The cone rotates to achieve the given shear stress (typically between 0 and $1.2s^{-1}$) and the rheometer software computes the shear viscosity according to:

$$\eta_{shear} = \frac{3\mathcal{T}}{2\pi R^3 \dot{\gamma}}, \tag{3.1}$$

where $\mathcal{T}$ is the torque on the plate, $R$ is the radius of the cone and $\dot{\gamma} = \omega/\theta_0$ is the shear rate [Mac94]. The results are plotted in figure 3-6. It allows to determine the zero-shear viscosity $\eta_o$ for each fluid, as given in table 3.3.

| **Angle** $\theta_0$ $[deg : min : sec]$ | 1 : 59 : 41 |
|---|---|
| **Radius** $R$ $[mm]$ | 40 |
| **Truncation** $[\mu m]$ | 50 |

Table 3.2: *Cone Properties*

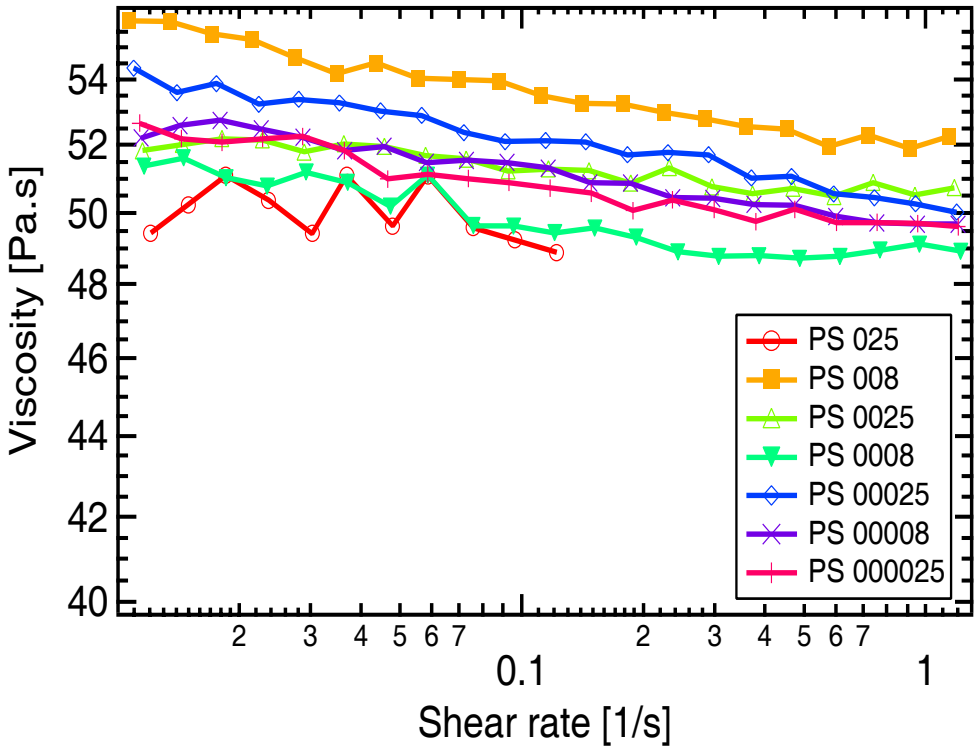


Figure 3-6: *Viscosity of diluted fluids as a function of shear rate.*

**Oscillatory shear flow: relaxation time**

The same cone is used to determine the relaxation times of the fluids. Several frequency sweeps are performed at various strains to cover the maximal range possible, roughly between 0.01 and $628 rad/s$. Let us consider a small-amplitude oscillatory shear flow: $\gamma(t) = \gamma_o \sin(\omega t)$. The shear rate is:

$$\dot{\gamma} = \gamma_0 \omega \sin(\omega t). \tag{3.2}$$

The shear stress response is given by:

$$\tau_{12} = G'(\omega)\gamma_0 \sin(\omega t) + G''(\omega)\gamma_0 \cos(\omega t), \tag{3.3}$$

where $G'$ and $G''$ are respectively the storage modulus and the loss modulus introduced in section 2.3.2.

Then, for each fluid a plot of storage modulus $G'$ and loss modulus $G''$ is obtained. Thanks to the Zimm theory (section 2.3.2), these points can be fitted. Shear rheology allows thus to calculate the relaxation time $\lambda_{SR}$, as shown on figure 3-7 for PS025.

When the dilution increases, the in-phase part of the signal becomes too weak to be correctly analyzed. This can be seen for example on figure 3-8 for PS00008 ($0.00008 wt.\%$ polystyrene). Therefore, it is impossible to fit the experimental data and then to calculate the relaxation time for fluids whose concentration is 0.00025% in weight or below.

The results of these experiments are in table 3.3.

| | **PS025** | **PS008** | **PS0025** | **PS0008** |
|---|---|---|---|---|
| **Zero-Shear Viscosity** $\eta_o$ $[Pa.s]$ | 49.0 | 55.7 | 52.0 | 52.0 |
| **Solvent Viscosity** $\eta_s$ $[Pa.s]$ | 45.5 | 55.3 | 51.7 | 51.9 |
| **Relaxation time** $\lambda_{SR}$ $[s]$ | 5.02 | 1.85 | 3.97 | 2.49 |

Table 3.3: *Results of shear rheology for the test fluids.*

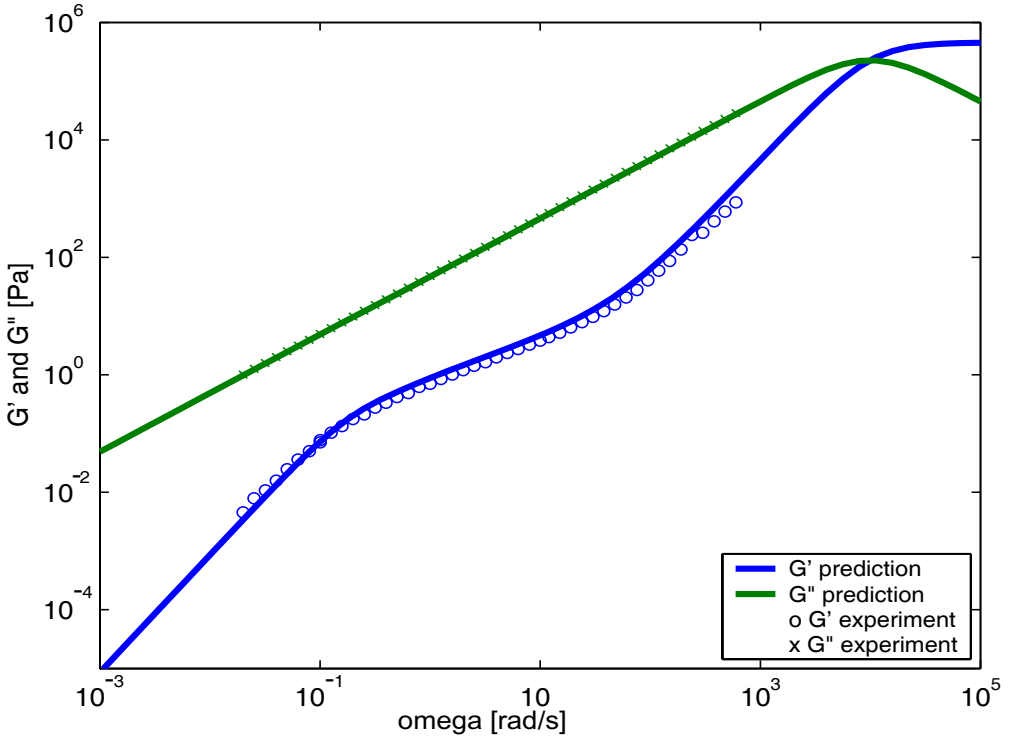


Figure 3-7: *Experimental values of storage and loss moduli fitted using Zimm theory for PS025 at* $25^0C$

### 3.3.2 Caber experiments

Experiments have been run using the Caber with the seven test fluids (PS025 diluted up to $0.000025wt.\%$). The "step strain experiment" is performed in $50ms$. This is the fastest the cylinder can open. The software returns the data collected by the laser micrometer: it consists in giving the value of the radius of the liquid filament as a function of time. A way of fitting the radius evolution data is to use a derived model interpretation. The expression given by McKinley (2000) is as follows:

$$R(t) = A - Bt + Ce^{-Dt} \tag{3.4}$$

with $D = 1/3\lambda_z$. Therefore, it is possible to measure the longest relaxation time $\lambda_z$ by fitting the experimental data and extracting the value $\lambda_z = 1/3D$.

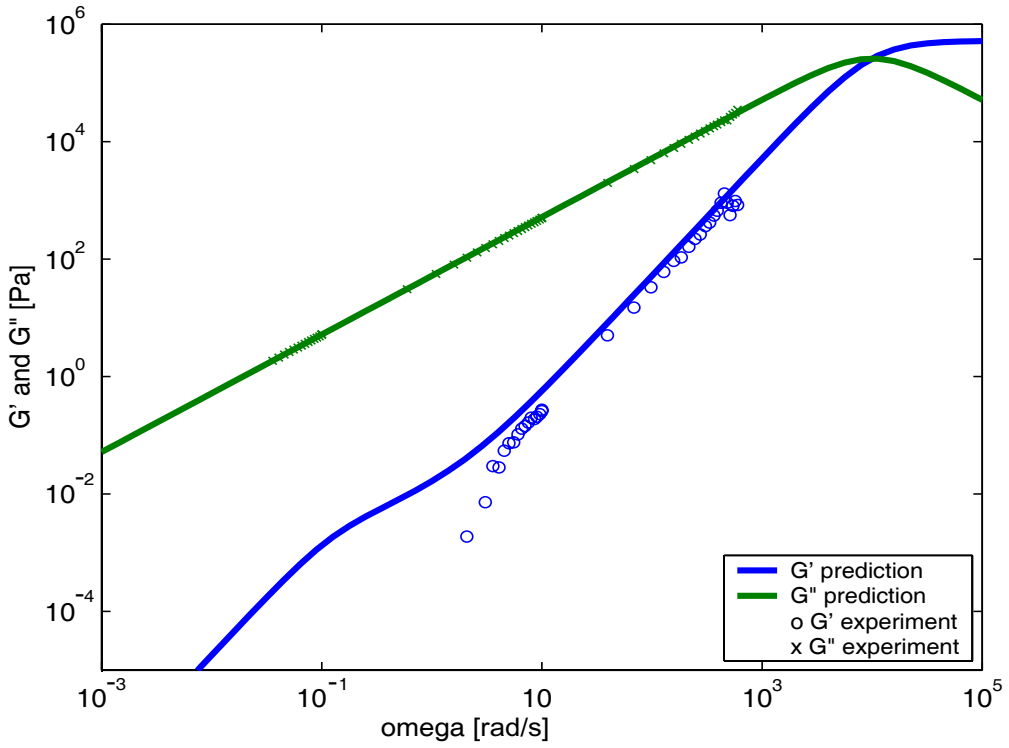


Figure 3-8: *Experimental values of storage and loss moduli fitted using Zimm theory for PS00008 at* $25^0C$

All these experiments are run at room temperature which could vary between $20^oC$ and $24^oC$. In order to have consistent results, one needs to shift all the results to a given temperature (chosen here to be $25^oC$) using a correction method: the time-temperature superposition ([Tan99] or [BAHC87]). From the equation 2.24 given in section 2.3.2, it can be seen that all the relaxation times $\lambda$ have the same dependence on temperature. We can then define a function $a_T(T_0)$ such as:

$$a_T(T_0) = \frac{\lambda(T)}{\lambda T_0} = \frac{\eta(T)}{\eta(T_0)}, \tag{3.5}$$

where $T_0$ is the arbitrary reference temperature. The shift factor $a_T(T_0)$ has been successfully fitted by the semi-empirical Williams-Landel-Ferry equation:

$$\ln(a_T) = \frac{-c_1^0(T - T_0)}{c_2^0 + (T - T_0)}, \tag{3.6}$$

in which $c_1^0$ and $c_2^0$ are experimentally determined constants [WLF55]. This equation is widely discussed by Ferry in [Fer80]. With the cone and plate rheometer AR1000 described in section 3.3.1, it is possible to perform a temperature ramp, for example between $20^oC$ and $35^oC$ and to measure the temperature-dependence of the viscosity. Then, this plot is fitted with the model of equations 3.5 and 3.6 as shown on figure 3-9 with the example of PS025. The WLF model fits very accurately with the experimental data. Knowing the relaxation time at the temperature of the experiment, we can then know it at any temperature thanks to the equation 3.5. It yields a natural scaling for the time scale $t/a_T(T_0)$ which allows us to compare the different experiments. The re-scaled experimental data for the text fluids is in figure 3-10 a) and b).

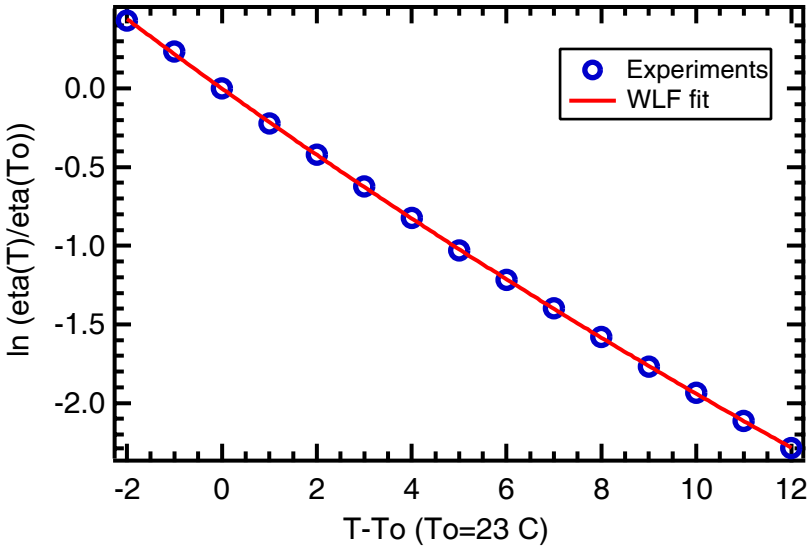


Figure 3-9: *Temperature-dependence of the viscosity of PS025 and fitting with WLF model.* $c_1^0 = 19.47 \pm 0.97$ *and* $c_2^0 = 90.31 \pm 4.95$.

In figure 3-10 a), we can characterize two different types of behaviors. The most concentrated fluid (PS025) shows mainly an exponential decrease, typical for a non-newtonian fluid. The beginning and the end of the stretching correspond to a linear decrease as can be seen better in figure 3-10 b). The most diluted fluids show a predominantly linear decrease in radius, which is a characteristic behavior for fluids

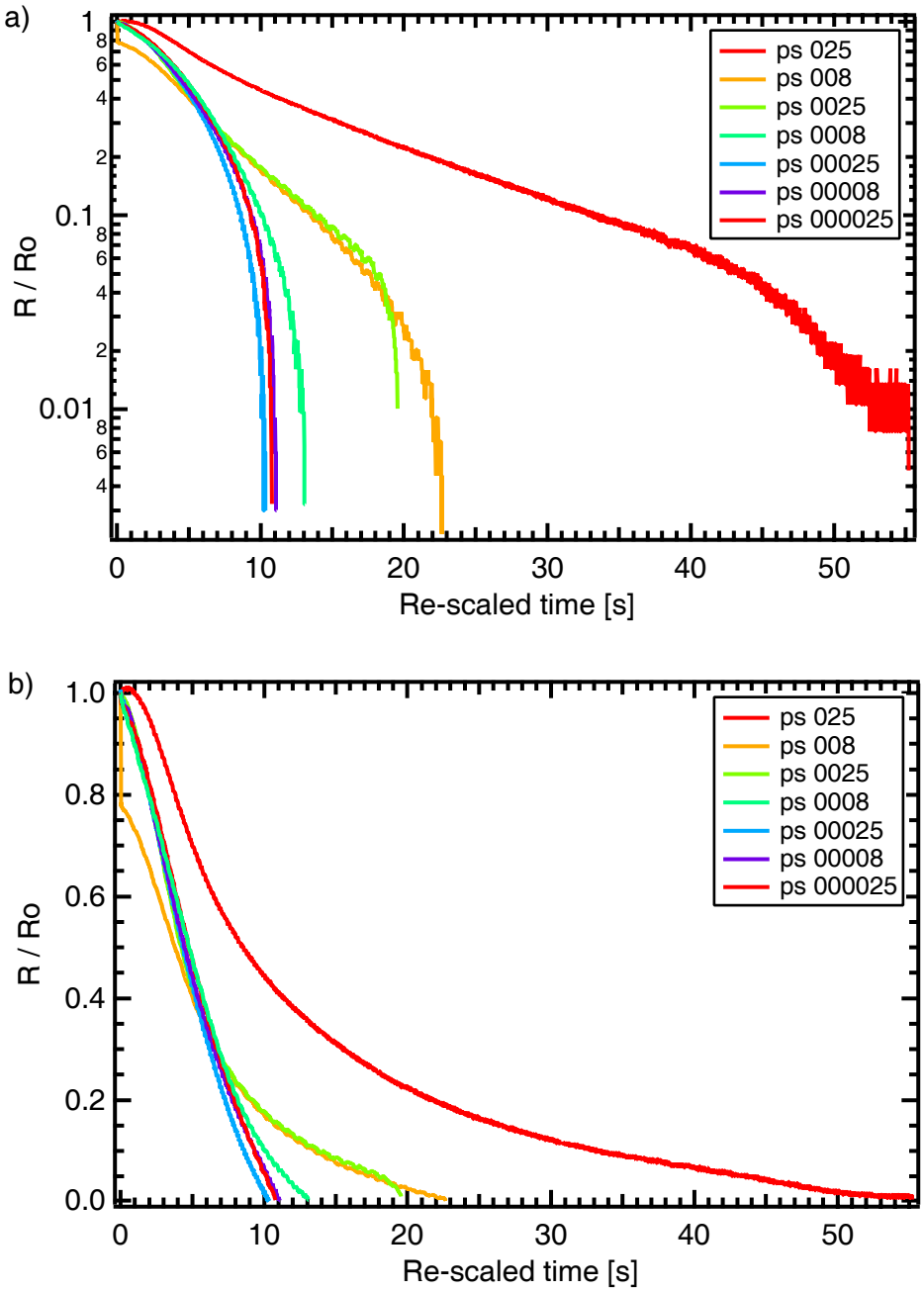


Figure 3-10: *a) Logarithmic plot of the radius decrease as a function of time for the test fluids. b) Linear plot of the radius decrease as a function of time for the test fluids.*

dominated by viscous forces. We try to explain this phenomenon in the next section. One can also note that PS025 takes a much longer time to break. Then, it tends to suggest that for concentrations such as $0.008wt.\%$ and below, test fluids behave more like Newtonian fluids during capillary break-up.

The results in terms of relaxation times derived by fitting of the experimental data and re-scaling are gathered in table 3.4.

### 3.3.3 Comparison with Kuhn Chain and Zimm models

The values for the relaxation times obtained by extensional rheology ($\lambda_{ER}$) can be compared to the relaxation times obtained by shear rheology with the Zimm theory ($\lambda_{SR}$) and by the equation 2.10 for the Kuhn Chain ($\lambda_{IV}$), as shown on table 3.4.

| **Conc.** $[wt.\%]$ | 0.025 | 0.008 | 0.0025 | 0.0008 | 0.00025 | 0.00008 | 0.000025 |
|---|---|---|---|---|---|---|---|
| $\lambda_{ER}$ $[s]$ | 4.17 | 1.98 | 1.98 | 1.97 | 1.95 | 1.86 | 1.80 |
| $\lambda_{SR}$ $[s]$ | 5.02 | 1.85 | 3.97 | 1.49 | | | |
| $\lambda_{IV}$ $[s]$ | 3.14 | 3.14 | 3.14 | 3.14 | 3.14 | 3.14 | 3.14 |

Table 3.4: *Comparison of longest relaxation times given by Zimm fitting, WLF fitting and Kuhn chain theory.*

Experimentally, we note a dependence of the relaxation time to the concentration of polymer in the fluid. According to the Kuhn chain model for dilute solutions, it should not depend on it (figure 3-11).

### 3.3.4 Profile of the filament

During Caber experiments, the form of the liquid filament bridge changes with time as it necks under the contributions of capillary, viscous and elastic stresses (equation 4.4). The caber is equipped with a micrometer which follows the evolution of the radius of liquid (section 3.1). It is also possible to record a movie of the thinning of the filament with a MS12 Cohu CCD camera. After an extraction of frames with the software Adobe Premiere 5.0, the edge of the filament is found by image analysis: it is

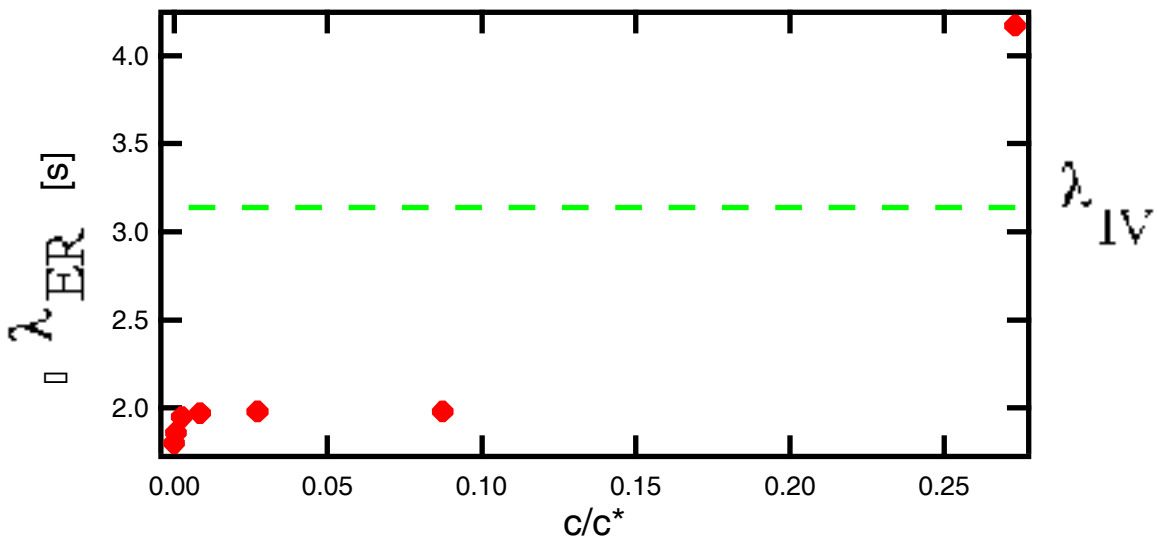


Figure 3-11: *Relaxation time ontained by extensional rheology as a function of the ratio $c/c^*$ for the test fluids. These values have to be compared with the relaxation time obtained by the Kuhn Chain model $\lambda_{IV}$.*

performed with the code *Caber Edgefinder by Christian Clasen4* written in Labview by Dr C. Clasen. The figure 3-12 shows an initial image and the output given by the Labview code. A plot superimposing the successive edges of the filament gives a qualitative idea of the behavior of the fluid (figures 3-13 and 3-14). In the absence of laser micrometer with the Caber, this image could also be used quantitatively. The sampling of the software gives a point every $50\mu m$ on the vertical axis, and the accuracy on the determination of the radius (radial measurement) should be about the same. Nevertheless, the fluids we use are transparent and a frame extracted from a movie is very often blurred. Then it is very difficult to digitize a precise shape. We note that the measurements of the radius extracted with this method are always smaller than the "real" values taken from the CABER data acquisition. This method is less reliable than the direct measure of the radius by the laser beam, but it gives a good idea of the form of the filament and of the behavior of the fluid.

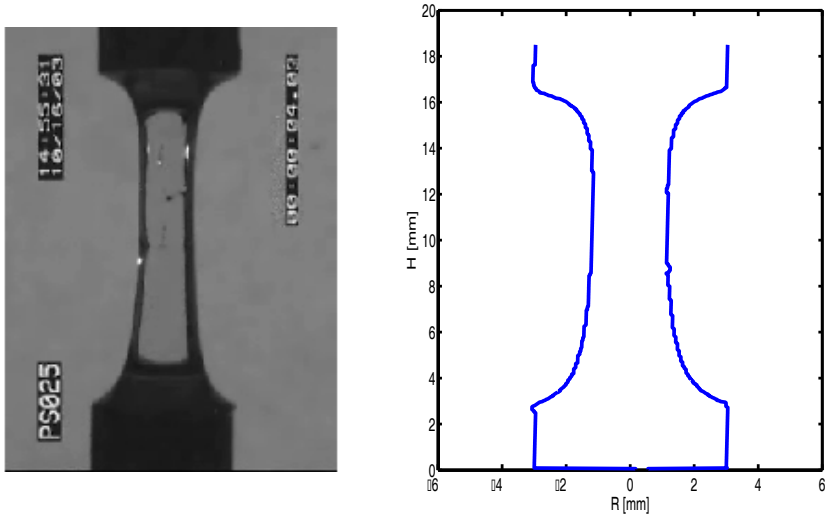


Figure 3-12: *Frame of a movie showing a liquid filament during the Caber experiment and digitized edge of this filament. The picture is taken right at the beginning of the necking process for the visco-elastic fluid PS025.*

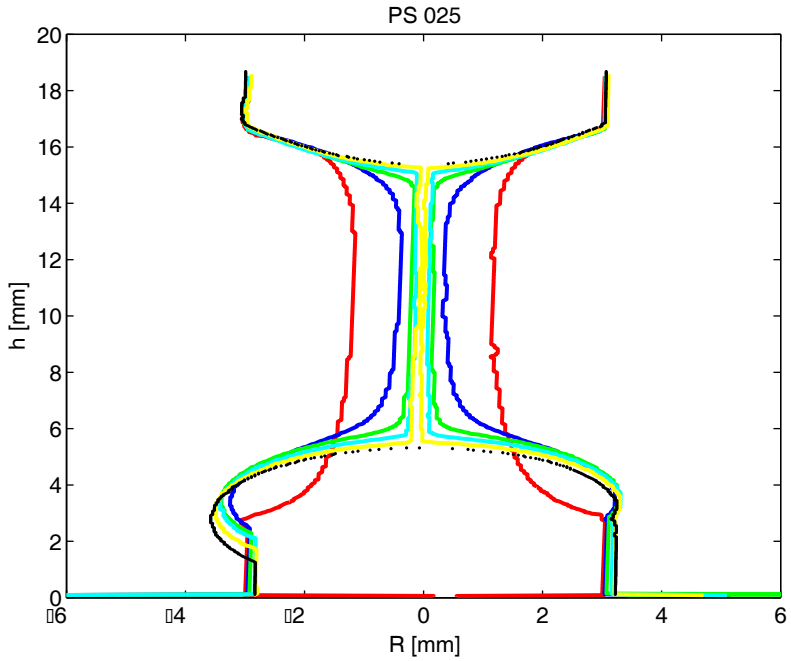


Figure 3-13: *Digitized edges of PS025 during a Caber experiment. The step of time between two profiles is 20s.*

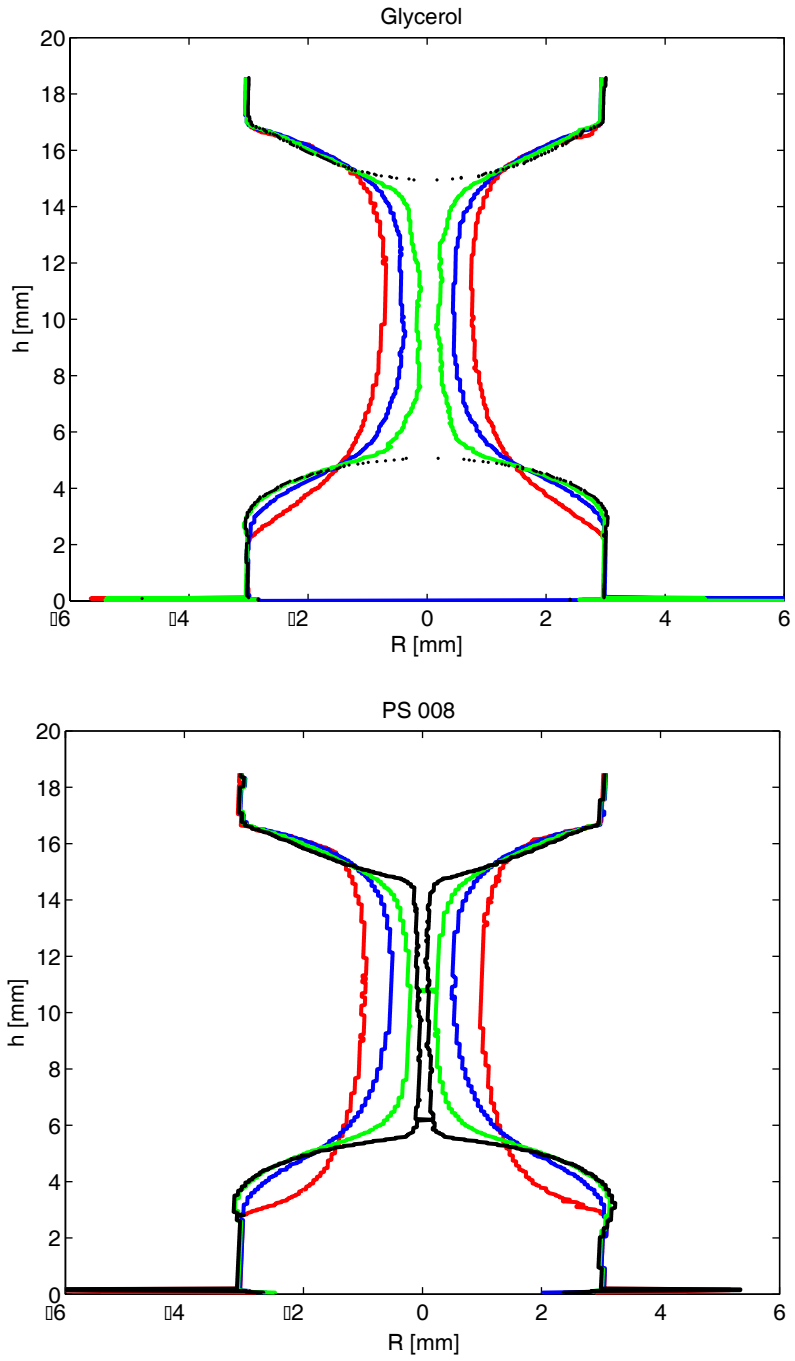


Figure 3-14: *Digitized edges of Glycerol and PS008 during a Caber experiment. The step of time between two profiles for glycerol and PS008 is respectively 50ms and 5s.*

## 3.4 Interpretation

**Elastic versus viscous effects:**

As discussed in section 2.3.1, the theoretical values of the longest relaxation time $\lambda_z$ and of the total viscosity of the solution $\eta_o = \eta_s(1+c[\eta]+...)$ are known. Then, we immediately can derive the ratio of the Deborah number over the Ohnesorge number $De/Oh$ to obtain the elasto-capillary number:

$$\frac{De}{Oh} = \frac{\lambda\sigma}{\eta_0 R_0} \tag{3.7}$$

$$\frac{De}{Oh} = \frac{1}{\zeta(3\nu)} \cdot \frac{[\eta]\sigma M_w}{N_A k_B T R_0(1+[\eta]c)} \tag{3.8}$$

According to the definition of these two dimensionless numbers, this ratio gives a measure of the relative size of elastic and viscous effects in the fluid. If this ratio is greater than one, the elastic effects are dominant; should it be otherwise, the fluid is dominated by viscous effects. The experimental data compared to the values obtained by shear rheology and Zimm fitting is summarized in figure 3-15.

These points are perturbed by the fact that the initial radius varies randomly from an experiment to another. Nevertheless, the two sets of experiments do enable us to see that the more concentrated fluid ($0.025 wt.\%$ polystyrene) has a ratio $De/Oh$ clearly greater than 1. For all of the other fluids, this ratio is around 1, i.e. considerably smaller. We have then two different types of behavior: a fluid dominated by elastic effects (PS025) and three fluids more or less clearly dominated by viscous effects. This explains what we observed in figure 3-10, i.e. a viscolelastic behavior of PS025 with a long phaes of exponential decrease of the radius, and a behavior dominated by viscous effects for all of the other fluids, with a predominantly linear decrease of the radius.

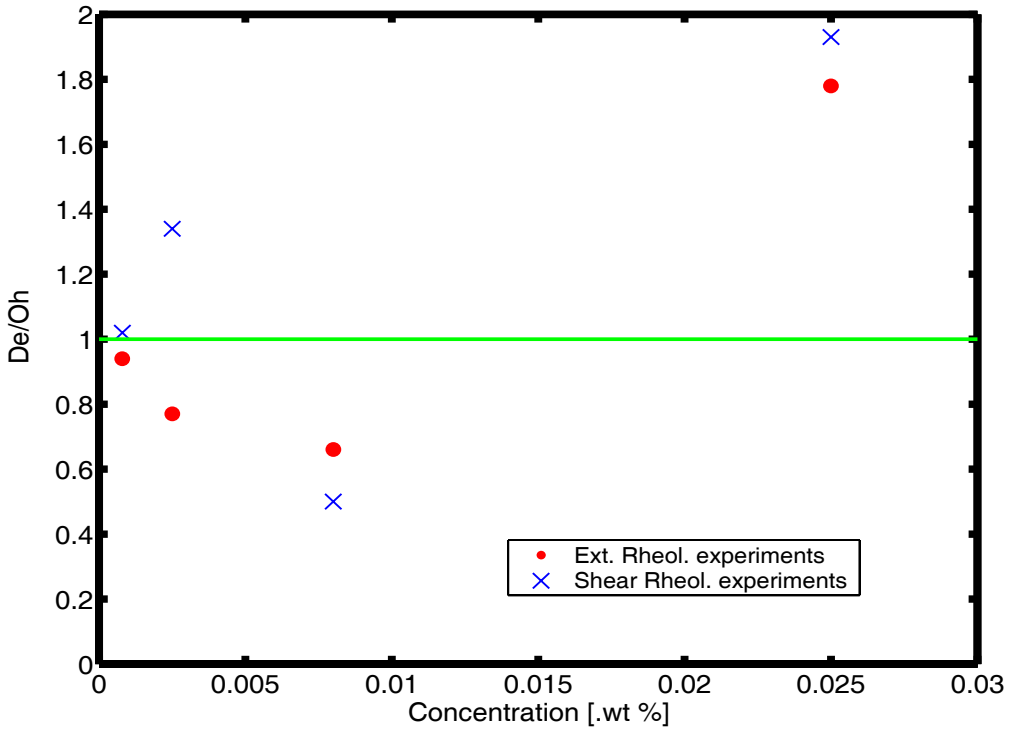


Figure 3-15: *Ratio of elastic over viscous effects as a function of the polymer concentration for shear rheology experiments and extensional rheology experiments. These results are for the fluids PS025, PS008, PS0025 and PS0008.*

# Chapter 4

# Caber simulation

## 4.1 Single-mode FENE fluid

### 4.1.1 Main equations

Analyzing the viscoelastic liquids in terms of a single-mode FENE fluid yields the following derivation, as discussed in Entov and Hinch for multi-mode FENE fluids [EH97]. Let consider an uniform cylindrical filament of radius $R(t)$ being squeezed by surface tension. The radius decreases according to the law $\dot{R} = -\frac{1}{2}\dot{\epsilon}R$, where $\dot{\epsilon}$ is the strain-rate of the axisymmetric extensional flow. The upper convected derivative of the deformation tensor $\underline{\underline{A}}$ obeys to the following equation:

$$\underline{\underline{A}}_{(i)} = -\frac{1}{\lambda}[f\underline{\underline{A}} - I], \tag{4.1}$$

with $\lambda$ the relaxation times and $f = \frac{1}{1-trA/L^2}$ the FENE factor for a finite extension $L$. $trA = A_{zz} + A_{rr} + A_{\theta\theta} = A_{zz} + 2Arr$

The axial deformation and the radial deformation of the FENE mode respectively satisfy the equations:

$$\dot{A_{zz}} = 2\dot{\epsilon}A_{zz} - \frac{1}{\lambda}(fA_{zz} - 1), \tag{4.2}$$

$$\dot{A_{rr}} = -\dot{\epsilon}A_{rr} - \frac{1}{\lambda}(fA_{rr} - 1). \tag{4.3}$$

The evolution of the liquid filament is given by the balance between capillary, viscous

and elastic stresses according to equation 4.4:

$$\frac{\sigma}{R} = 3\eta_s \left( -2\frac{d\ln R}{dt} \right) + (\tau_{zz} - \tau_{rr}), \tag{4.4}$$

where $\tau_p = [\tau_{zz} - \tau_{rr}] = Gf(A_{zz} - A_{rr})$ is the normal stress difference for a single-mode FENE fluid and $G = nk_BT = cN_Ak_BT/M_w$ is the elastic modulus.

At early times, the viscous response of the solvent is not negligible for dilute polymer solutions. Hence, the initial value of the axial stretch at the end of the imposed stretching and beginning of capillary thinning has to be chosen non-equal to zero. Entov and Hinch [EH97] agreed on the importance of initial stress to determine the initial conditions when comparing their computations with the experiments of Liang and Mackley [LM94]. Taking this into account, Anna and McKinley [AM01] proposed the following equation for the initial axial deformation:

$$A^0_{zz} = \frac{\sigma}{GR} - \frac{2\eta_s}{G\lambda_z}. \tag{4.5}$$

The polymeric stretch subsequently grows exponentially according to $A_{zz}(t) = A^0_{zz}e^{t/3\lambda_z}$. This growth rate explains why a right choice for the initial value is crucial in a numerical simulation. The other initial condition is that of an undeformed material: $A_{rr}(t = 0) = 1$.

### 4.1.2 Numerical solutions

A simulation of a filament thinning has been done for several concentrations of polymer fluid. The simulated fluid was styrene oil with, respectively 0.025, 0.008, 0.0025, and 0.0008% of polystyrene in weight. The simulation code is written in Matlab. The inputs of this code are the relaxation time (derivated from the Kuhn theory trough equation 2.10), the solvent viscosity, the solution viscosity and some physical parameters (surface tension $\sigma$, density $\rho$, finite extensibility $L^2$). Typical inputs are given in table 4.1. The initial axial deformation is arbitrarily chosen: $A^0_{zz} = 1$ .The results, compared to the experimental data, are gathered in figure 4-1.

The less diluted fluid PS025 clearly does not behave as the more diluted: the

| **Fluid** | PS025 | PS008 | PS0025 | PS0008 |
|---|---|---|---|---|
| $\lambda$ $[s]$ | 5.02 | 1.85 | 3.97 | 2.49 |
| Solvent visc. $\eta_s$ $[Pa.s]$ | 45.5 | 55.3 | 51.7 | 51.9 |
| Total visc. $\eta_0$ $[Pa.s]$ | 49 | 55.7 | 52 | 52 |
| Surf. tension $\sigma$ $[mN/m]$ | 38 | 38 | 38 | 38 |
| Density $\rho$ $[kg/m^3]$ | 1026 | 1026 | 1026 | 1026 |
| Extensibility $L^2$ | 4606 | 4606 | 4606 | 4606 |

Table 4.1: *Inputs used for numerical simulations: physical characteristics of the four fluids to be simulated.*

breakup time (divided by the relaxation time of the fluid) is much longer and the filament necking looks exponential, whereas other fluids seem to behave more or less like Newtonian fluids (fast breakup time, linear necking). These two different behaviors can be qualitatively perceived on the pictures showing the necking process for fluids whose concentrations are respectively $0.025wt.\%$ and $0.008wt.\%$ (figures 4-2.

The force balance during the filament stretching, corresponding to equation 4.4, is shown on figures 4-3 and 4-4 respectively for a moderately diluted solution (PS025) and a highly diluted solution (PS0025). The different stretching behaviors stated in figure 4-1 are clearly explained by these two force balances: in the case of the less diluted fluid, the elastic stress increases and finally equilibrates the capillary stress, while the viscous stress tends to a constant value $3\eta_s\dot{\epsilon} \approx 2\eta_s/\lambda$, as in elasto-capillary thinning the necking filament selects a natural scale $\dot{\epsilon} \approx 2/(3\lambda)$ [AM01]. In the case of the more diluted fluid, capillary stress is balanced by viscous stress. Then, the fluid behaves like a simple viscous fluid and the radius of the filament decreases linearly as for a Newtonian fluid. This confirms what is observed in figure 4-1.

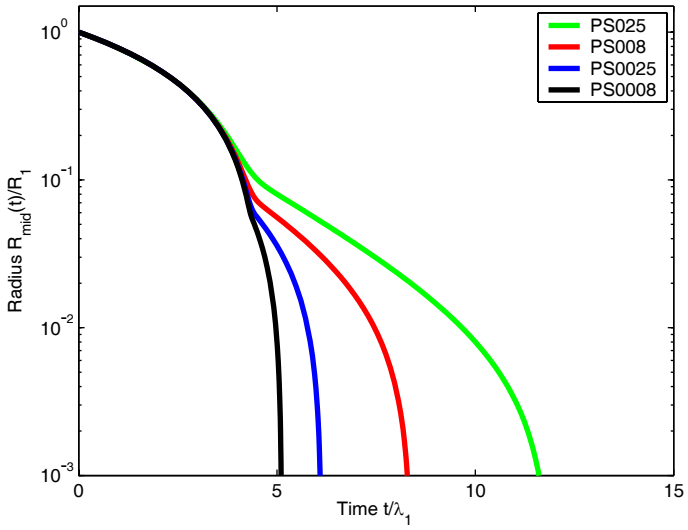


Figure 4-1: *Simulated behaviors of the fluids described in table 4.1.*

## 4.2 Asymptotic behaviors of an elastic fluid

### 4.2.1 Visco-capillary (VC) balance

Our main assumption is of strong surface tension $\sigma/R >> G$, what is justified by the weak polymer concentrations we consider. At early times, it means that we start with no elastic stress. We then have a balance between only capillary forces and viscous forces due to the solvent viscosity. The equation of the force balance reduces to:

$$\frac{\sigma}{R} = 3\eta_s\dot{\epsilon}. \tag{4.6}$$

The radius satisfies then the differential equation 4.7:

$$\frac{dR}{dt} = -\frac{\sigma}{6\eta_s}t. \tag{4.7}$$

Integrating this equation yields linear time dependence: $R(t) = R_1 - \frac{\sigma}{6\eta_s}t$. This is the behavior we usually observe with Newtonian fluids. Capillary stress is then given by:

$$\frac{\sigma}{R} = \frac{\sigma}{Ro - \frac{\sigma}{6\eta_s}t}. \tag{4.8}$$

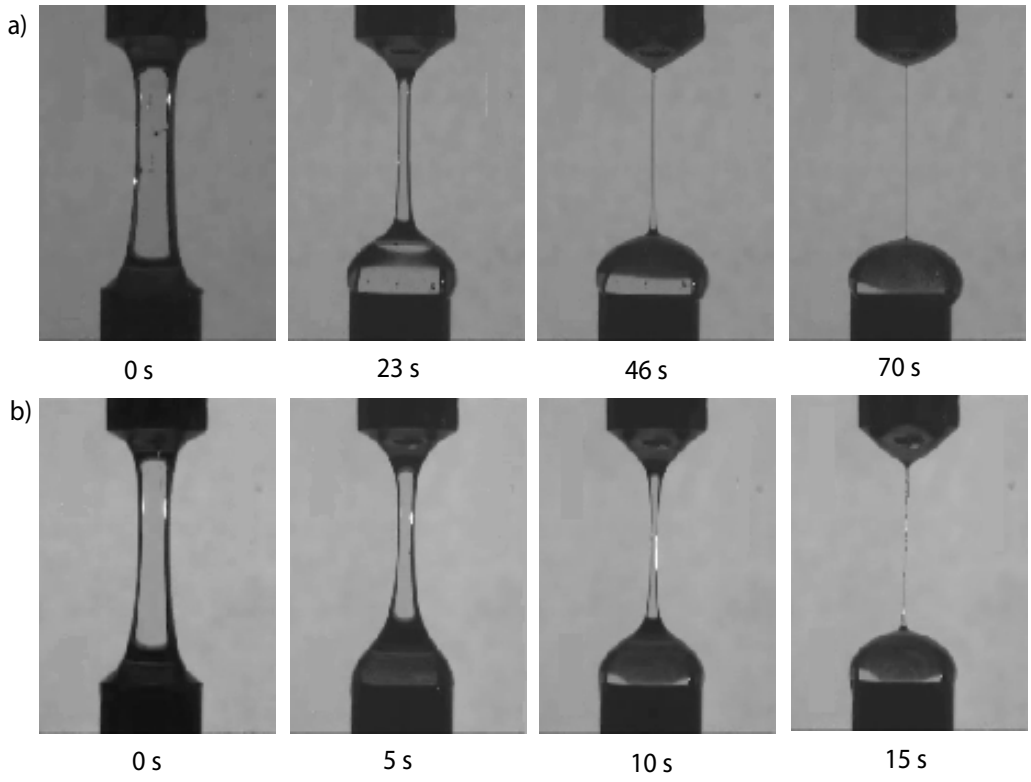


Figure 4-2: *a) Filament necking for a moderately diluted solution of* $0.025wt.\%$ *polystyrene in styrene oil (PS025 described in table 4.1). b) Filament necking for a diluted solution of* $0.008wt.\%$ *polystyrene in styrene oil (PS008 described in table 4.1).*

The polymer chain stretching yields an increase of the elastic stress, which eventually becomes comparable to the capillary and viscous stresses. Viscous stress then drops with the strain-rate in order for the elastic stress not to increase beyond the capillary stress.This phase change leads to the elasto-capillary part of the filament necking.

### 4.2.2 Elasto-capillary (EC) balance

In this limit, the force balance satisfies the following equation:

$$\frac{\sigma}{R} = (\tau_{zz} - \tau_{rr}). \tag{4.9}$$

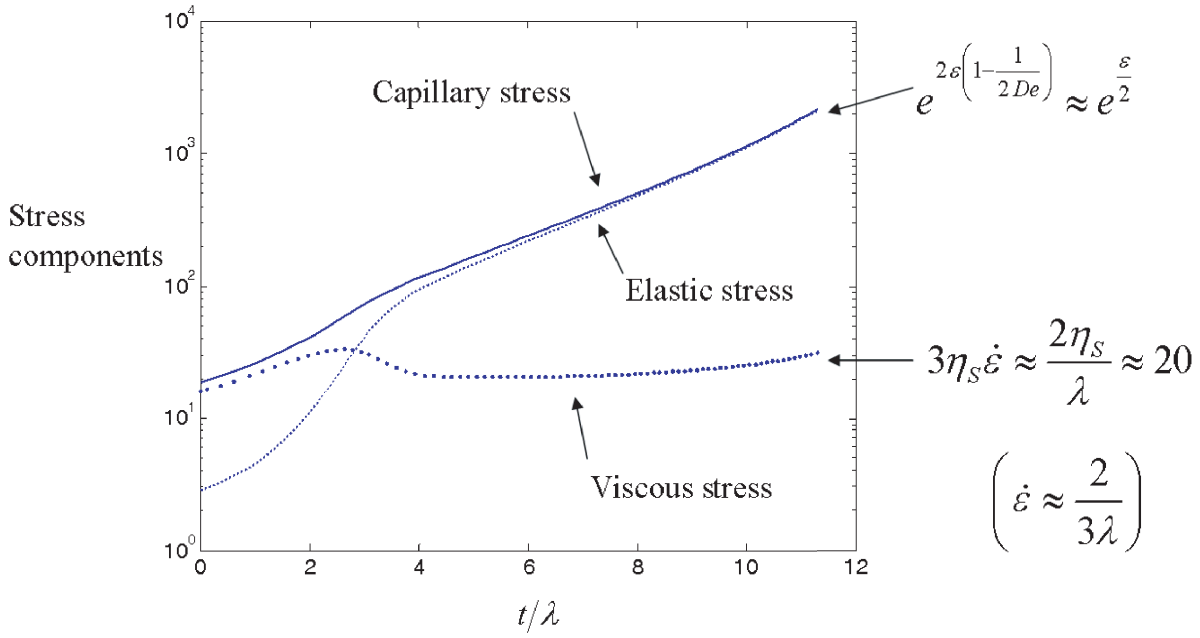


Figure 4-3: *Force balance during stretching for a moderately diluted solution (PS025: 0.025wt.% polystyrene in styrene oil described in table 4.1).*

We focus our study here on deformations smaller than the finite extension limit ($A_{zz} << L^2$). We assume that deformations are important ($A_{zz} >> 1$) and FENE factors are taken equal to 1 (Hookean model). Equation 4.1 gives in this case:

$$\lambda \frac{d \ln A_{zz}}{dt} + 4 \frac{d \ln R}{dt} = -\frac{1}{\lambda}. \tag{4.10}$$

The axial deformation equation can be integrated as:

$$A_{zz}(t) = A_{zz}^0 \left(\frac{Ro}{R(t)}\right)^4 e^{-t/\lambda}. \tag{4.11}$$

The elastic stress is $\tau_{zz} = G(fA_{zz} - 1) \approx GA_{zz}$. So the balance of the stresses 4.9 becomes:

$$\frac{\sigma}{R} = GA_{zz}^0 \left(\frac{Ro}{R}\right)^4 e^{-t/\lambda}. \tag{4.12}$$

This finally gives exponential time dependence for the radius:

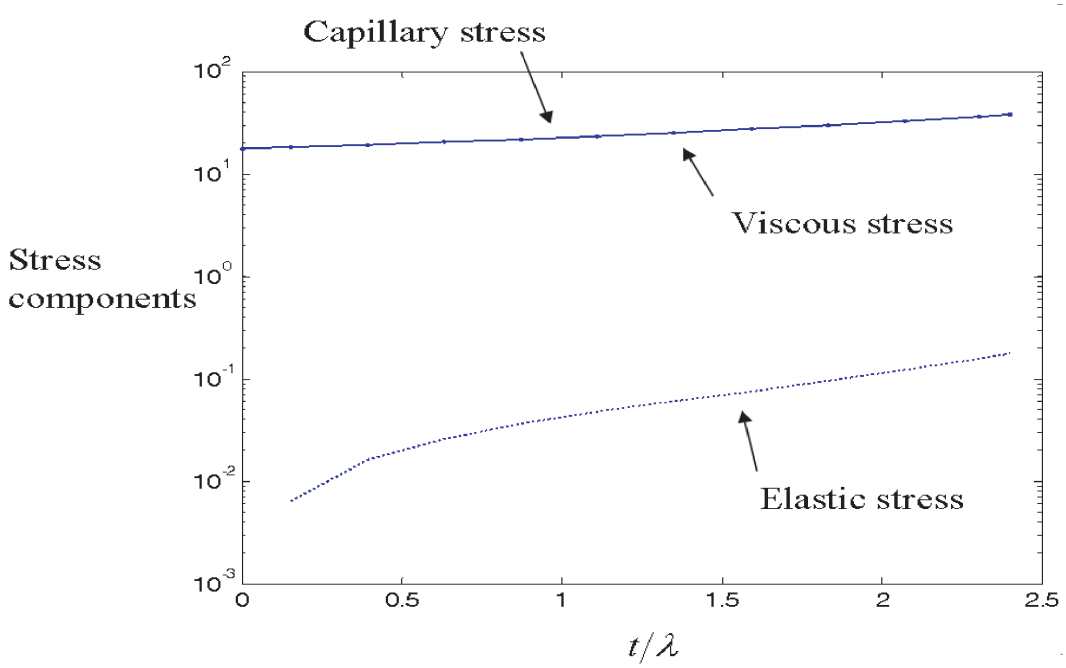


Figure 4-4: *Force balance during stretching for a highly diluted solution (PS0025:* 0.0025*wt.% polystyrene in styrene oil described in table 4.1).*

$$R(t) = Ro\left(\frac{GA_{zz}^0 Ro}{\sigma}\right)^{\frac{1}{3}} e^{-\frac{t}{3\lambda}}. \tag{4.13}$$

EC stress balance is then expressed by the following equation:

$$\frac{\sigma}{R} = \tau_{zz} = \frac{\sigma}{Ro\left(\frac{RoGA_{zz}^0}{\sigma}\right)^{1/3}} e^{\frac{t}{3\lambda}}. \tag{4.14}$$

A good approximation of the time when the phase change occurs is given by the intersection between the asymptotic VC and EC behaviors. As the deformation keeps increasing, the finite extension limit $L$ has finally an effect on the necking. This can be represented by a third asymptotic behavior iof the fluid.

### 4.2.3 Fully Extended (FE) limit

Viscous stress is then a difference of large numbers and the system of equations 4.1 becomes very stiff. Once the viscous stress is small, we have a balance between

capillary and elastic stresses. FENE factors are no longer taken equal to 1. $trA = A_{zz} + A_{rr} + A_{\theta\theta} \approx A_{zz}$ as $A_{zz} >> A_{rr} \approx 1$ At the late times of finite extension, the rate of increase in the deformation is negligible. Thusm the solution of 4.1 can be approximated to the steady-state solution:

$$2\dot{\epsilon}\lambda A_{zz} = fA_{zz}. \tag{4.15}$$

So, the solutions are:

$$f = 2\dot{\epsilon}\lambda, \tag{4.16}$$

$$A_{zz} = L^2\left(1 - \frac{1}{2\dot{\epsilon}\lambda}\right). \tag{4.17}$$

The elastic stress is $\tau_{zz} = G(fA_{zz} - 1) \approx 2G\lambda L^2\dot{\epsilon}$. The FENE fluid is now behaving like a suspension of rigid rods, with an effective viscosity $\eta^*$ such as $3\eta^* = 2G\lambda L^2$. Hence, as in VC behavior, the radius has linear time-dependence:

$$R(t) = \frac{\sigma}{6\eta^*}(t_b - t), \tag{4.18}$$

where $t_b$ is the (unknown) time when the filament breaks.

The stress balance is then given by:

$$\frac{\sigma}{R} = \frac{6\eta^*}{t_b - t}. \tag{4.19}$$

Therefore, for a numerical simulation based on these equations, we expect three consecutive asymptotic behaviors for the radius as a function of time: linear, exponential and linear again.

## 4.3 Comparison with numerical solutions

The main goal here is to find a criteria on parameters, such as the finite extensibility $L$ or the molecular weight of the polymer diluted in the viscous solvent $M_w$, to determine whether or not we can observe the Non-Newtonian behavior of a given fluid with Caber experiments.

### 4.3.1 Correspondence between numerical integrations and asymptotic results

Numerical simulations are run using the same parameters as in section 4.1.2 for the fluid PS025. They are recalled in table 4.2.

| | |
|---|---|
| **Concentration** $[wt.\%]$ | 0.025 |
| **Solvent viscosity** $\eta_s$ $[Pa.s]$ | 45 |
| **Surface tension** $\sigma$ $[mN/m]$ | 38 |
| **Density** $\rho$ $[kg/m^3]$ | 1026 |

Table 4.2: *Inputs for simulations of stress balances of a polymer solution.*

| | |
|---|---|
| **FENE-P model** | $\frac{\sigma}{R} = 3\eta_s\left(-2\frac{d\ln R}{dt}\right) + (\tau_{zz} - \tau_{rr})$ |
| **Visco-capillary balance** | $\frac{\sigma}{R} = \frac{\sigma}{Ro - \frac{\sigma}{6\eta_s}t}$ |
| **Elasto-capillary balance** | $\frac{\sigma}{R} = \frac{\sigma}{Ro\left(\frac{RoGA^0_{zz}}{\sigma}\right)^{1/3}e^{\frac{t}{3\lambda}}}$ |
| **Fully Extended limit** | $\frac{\sigma}{R} = \frac{6\eta^*}{t_b - t}$ with $\eta^* = \frac{2}{3}G\lambda L^2$ |

Table 4.3: *Main equations of the asymptotic approach. Recall from section 4.2.*

The results of the simulations for four different molecular weights are done on figure 4-5. This figure represents the balance of stresses for the fluids during the process of filament necking, and the three asymptotic behaviors described in section 4.2. The main equations of this problem are recalled in table 4.3.

For all the fluids, the three asymptotic behaviors match pretty well with the numerical data. So, it allows to explain the process of necking and the successive balances of stresses in the filament of fluid. At first, the elastic stress is negligible compared to viscous and capillary stresses. The numerically-computed capillary stress follows the asymptotic VC part (equation given in table 4.3 and dashed red line on figure 4-5), and the numerically-computed elastic stress is smaller of several orders of magnitude. The fluid behaves as a Newtonian fluid and the radius of the filament of fluid decreases linearly with time. This statement is true for every molecular weight.

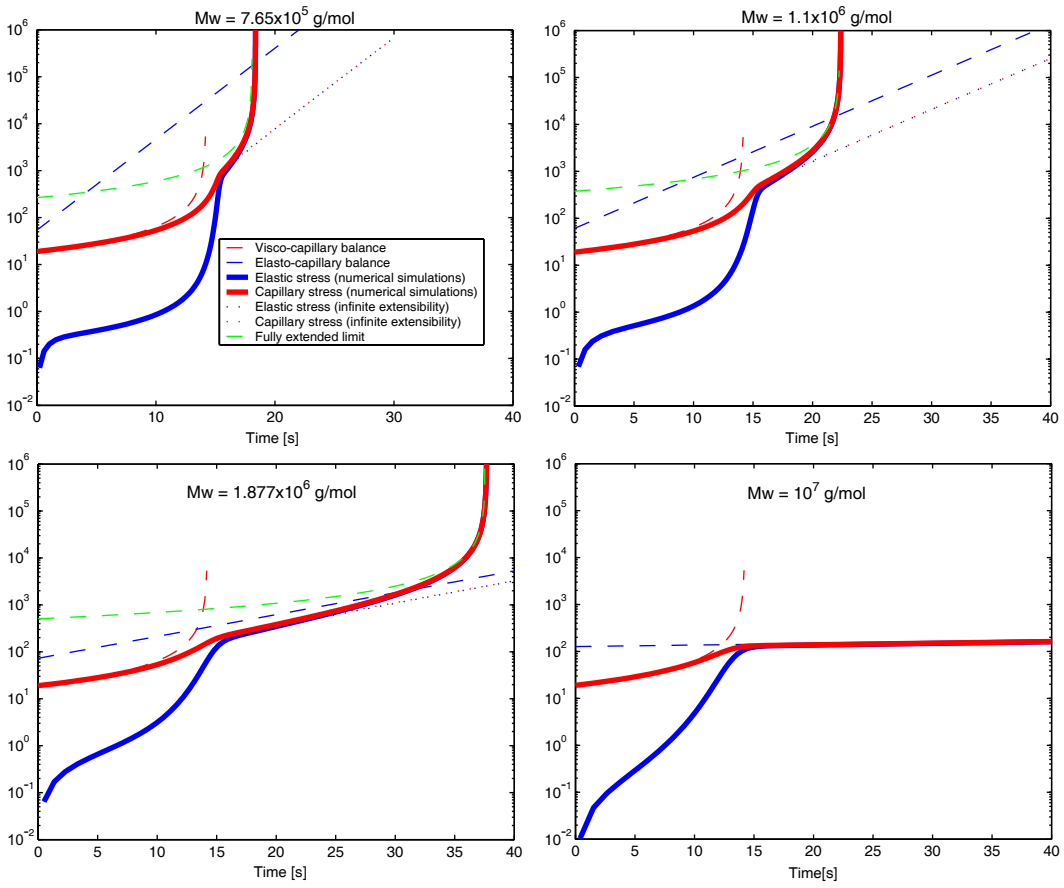


Figure 4-5: *Simulated balance of stresses and asymptotic approximations for a solution of polystyrene with a concentration of* $0.025wt.\%$ *polystyrene in styrene oil (described in table 4.2). The molecular weight of the polymer is successively taken equal to* $7.65 \times 10^5\ g/mol$, $1.1 \times 10^6\ g/mol$, $1.877 \times 10^6\ g/mol$ *and* $10^7\ g/mol$.

Then, the elastic stress grows up and finally becomes dominant over the viscous stress: the numerical simulation matches with the EC part (equation given in table 4.3). It can be approximated by a balance between capillary and elastic stresses only. This part of the curve corresponds to an exponential decrease of the radius of the filament of liquid as $e^{-\frac{t}{3\lambda}}$. The slope of the asymptotic curve (the dashed blue line on figure 4-5)corresponds to the simulation for large values of the molecular weight ($M_w = 10^7\ g/mol$). For smaller values of molecular weight, like $M_w = 7.65 \times 10^5$ $g/mol$ or even $M_w = 1.1 \times 10^6\ g/mol$, the polymer chains are shorter. They are more quickly fully extended. The balance between capillary and elastic stress is too short to be clearly observed, and so the numerical curves are never parallel to the asymptotic estimate. For $M_w = 1.877 \times 10^6\ g/mol$, the slope of the numerical data is not exactly the same as the slope of the asymptotic line. The difference comes from the neglected term in the equation 4.20:

$$\lambda \frac{d \ln A_{zz}}{dt} + 4 \frac{d \ln R}{dt} = -\frac{1}{\lambda} - \frac{\mathbf{1}}{\mathbf{A_{zz}}}. \tag{4.20}$$

This additional term modifies the slope of the simulation and explains why the simulation and the estimate are never parallel in that case. This elasto-capillary balance has been exaggerated on figure 4-5 by superimposing a plot of the numerical simulation with an infinite extensibility $L$. This is the part we want to be able to observe with the Caber because we can extract the relaxation time from its fitting.

As seen before, the extensibility is finite and finally the curve adopts the fully extended (FE) asymptotic behavior (dashed green line on figure 4-5) in the cases of the three smallest molecular weights. The radius decrease in this part of the filament necking is once again linear and corresponds to the equation given in table 4.3. For $M_w = 10^7\ g/mol$, the chain is much longer and therefore it is never fully extended. So the numerical simulations remain very well described by the elasto-capillary balance.

Thanks to the simulations run to plot the figure 4-5, we see that, depending on the molecular weight of the polymer, the EC part is more or less stressed. Clearly, it will be easier to observe it when the molecular weight is big enough. The limit of observability seems to be around $M_w = 1.1 \times 10^6 g/mol$. For smaller values, the

EC part is too short. The three asymptotic regimes appear as a good description of the phenomena involved in the filament necking. They also allow to find a criterion on the molecular weight for the observation of the elasto-capillary regime during the necking of a filament of liquid in the Caber. Nevertheless for two different reasons this does not appear as an instrument of prediction of the phenomena. First, the EC estimate predicts the slope of the numerical integrations, but its origin depends on the initial axial deformation $A^0_{zz}$ which is unknown. The intersection between the dashed red and the dashed blue lines on figure 4-5 does not give the point where the regime changes as we wish. Then, the estimate of the fully extended limit is plotted backward in taking the value of the break-up time $t_b$ from the numerical results (equation 4.19). There are formulas which predict this value, but their accuracy has not yet be proved ([EH97]).

### 4.3.2 Observation of the Non-Newtonian behavior

Just after the step strain by the Caber, the radius of a filament of fluid is typically around $2mm$. The accuracy of the laser micrometer which measures this radius on the Caber is $10\mu m$. Therefore, the observable range on the Caber data is no more than two orders of magnitude. If we want to find a criteria to determine if the exponential decrease of the radius is visible for a Caber experiment with a given fluid thanks to numerical simulations, we then have to restrain to two orders of magnitude for the radius.

#### Characteristic time scales

During the necking, two phenomena with different time scales are in competition and the appearance of Non-Newtonian effects depends on the ratio of these time scales. The polymer chain reacts in a time of the order of the relaxation time $\lambda$ and it is the source of non-newtonian effects. The viscous effects of the solvent define a natural time scale $\frac{\eta_s Ro}{\sigma}$. The ratio is then:

$$\delta = \frac{\lambda}{\eta_s Ro/\sigma}. \tag{4.21}$$

The ratios of these characteristics times of the simulated fluids are gathered in table 4.4:

| **Molecular weight** $[g/mol]$ | $7.65 \times 10^5$ | $1.1 \times 10^6$ | $1.877 \times 10^6$ | $10^7$ |
|---|---|---|---|---|
| $\delta$ | 0.315 | 0.562 | 1.313 | 18.78 |

Table 4.4: *Ratio of the characteristic time scales for different molecular weights of the polymer.*

### Variation of the solvent viscosity

Decreasing the solvent viscosity $\eta_s$ for everything else taken constant yields a decrease of the characteristic viscous time described in section 4.3.2. Nevertheless, the Kuhn chain theory states that the relaxation time of the chain $\lambda$ is proportional to the solvent viscosity (equation 2.10). Hence, the parameter $\delta$ defined in the section 4.3.2 does not change when the solvent viscosity changes. According to previous comments, a variation of viscosity does not help the observation of the Non-Newtonian part of stretching (EC part described in section 4.2.2). We can observe this phenomenon on the following simulated curves of the radius as a function of real time (figure 4-7). As shown on figure 4-6 for $M_w = 1.877 \times 10^6\ g/mol$, the curves superimpose if plotted as as a function of the adimensional time $t/\lambda$. Therefore for a given molecular weight of the polymer, all the curves on figure 4-7 are self-similar and the value of the radius for which there is the transition between VC and EC remains the same.

According to the figure 4-7, the exponential decrease of the radius is observable in the given conditions (table 4.2) only for polymers with a molecular weight bigger than about $10^6 g/mol$. This statement is in good agreement with the conclusion of the section 4.3.1.

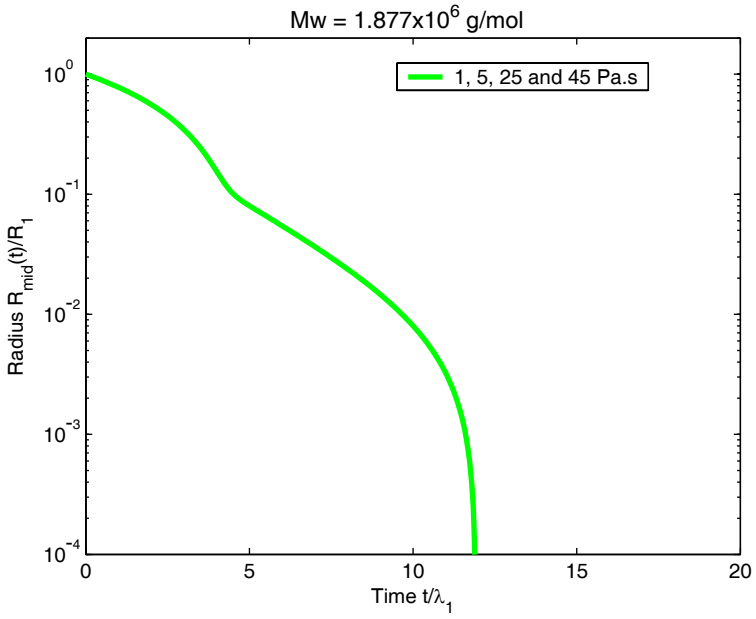


Figure 4-6: *Radius decrease for solvent viscosity of 1, 5, 25 and 45 Pa.s as a function of the reduced time $t/\lambda$ for a solution of polystyrene described in table 4.2 with a molecular weight of $M_w = 1.877 \times 10^6$ $g/mol$.*

### 4.3.3 Conclusion

The numerical simulations led with Matlab can be explained by three successive balances of stresses corresponding to three phenomena easily explained. It also allows us to qualitatively determine in advance if a polymer solution will demonstrate a visible Non-Newtonian behavior. A more quantitative way which is in good agreement with the simulations is the ratio of characteristic times $\delta$ (section 4.3.2). It seems that the exponential decrease of the radius is observable for $\delta$ being equal or greater than 1. The more $\delta$ is big, the easiest will be the observation of the exponential part. Finally, we also noticed that a variation of the solvent viscosity can not be used to facilitate the observation of the elasto-capillary part, as its effects in the relaxation time and the viscous time are perfectly opposed.

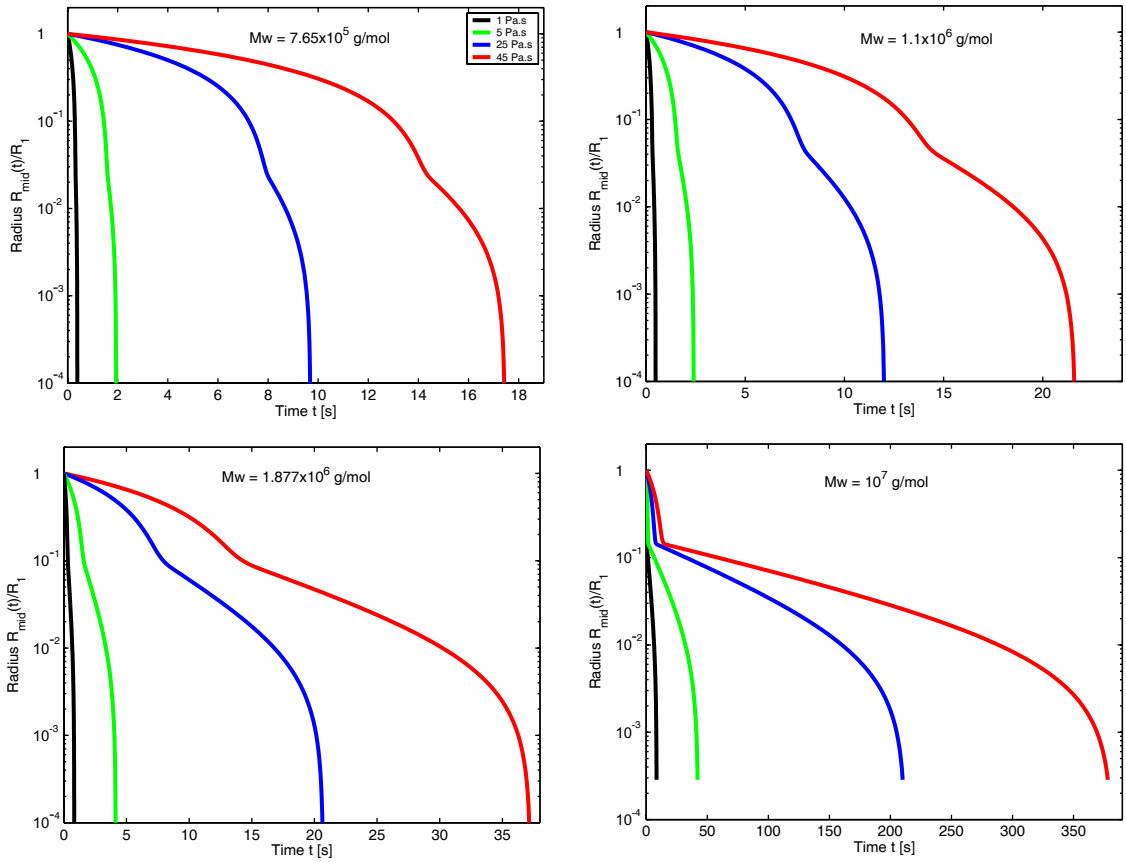


Figure 4-7: *Radius decrease for different solvent viscosities (1, 5, 25 and 45 Pa.s) as a function of real time. The fluid characteristics are given in table 4.2.*

# Chapter 5

# Characterization of New Elastic Test Fluid

In the previous study of the visco-elastic fluid PS025 and its derivatives, we have neglected the gravity in the force balance (equation 4.4). Nevertheless, the profile of the filament during the necking process let appear a gravitational sag on the bottom plate of the CABER. It is then interesting to run the CABER experiments with a visco-elastic fluid less susceptible to gravity. The preparation and the characterization of such a fluid are exposed in the following part.

## 5.1 Gravitational effects

As seen in section 2.4, in filament stretching rheometry several dimensionless groups can characterize an experiment. The Bond number is given by the equation 2.33. It describes the competition between gravity and surface tension. This number is a measure of the axial asymmetry of the initial static fluid column about its mid-plane. Another dimensionless group is the capillary number $Ca$. It expresses the competition between viscous forces and surface tension, and it is given by equation 2.34. For Newtonian fluids at least, the capillary number is a measure of the stability of the slender fluid filament as it is stretched. Viscous forces tend to stabilize the cylindrical shape, while surface tension acts to destabilize the shape by causing the

diameter to rapidly decrease until the filament breaks apart. The ratio of the Bond number to the capillary number is then important because it reveals the competition between gravitational and viscous forces during stretching:

$$\frac{Bo}{Ca} = \frac{\rho g R_0}{\eta_o \dot{\epsilon_o}} \tag{5.1}$$

A large value of this ratio indicates that a significant amount of fluid drains below the mid-plane of the filament during stretching. If $Bo/Ca$ is large enough, it leads to an additional correction term in the force balance of the form:

$$\frac{\rho g \delta V}{\pi R_{mid}^2} \tag{5.2}$$

where $\delta V$ is the extra volume below the mid-plane. The evolution of this incremental volume with time is a complicated function of surface curvature and cannot be computed analytically even for a Newtonian filament. But this term can become important for large enough $Bo/Ca$ values, and then equation 5.2 has to be taken into account. The experimental conditions for which gravitational sagging will become important can be estimated using dimensionless quantities. Since gravitational forces begin to dominate when $Bo/Ca$ approaches unity, equation 5.1 can be used to compute a critical strain rate below which sagging becomes important:

$$\dot{\epsilon_{sag}}(T) = \frac{\rho g R_o}{\eta_o a_T T/T_o} \tag{5.3}$$

where $a_T$ is the Williams-Landel-Ferry shift factor [Tan99]. The condition 5.3 leads to a critical Deborah number, $De_{sag}$ , which depends only on temperature, material properties and test geometry:

$$De_{sag}(T) = \lambda_z(T_o)\frac{\rho g R_o}{\eta_o}\frac{T_o}{T} \tag{5.4}$$

Values of $De_{sag}$ can be evaluated for each filament stretching rheometer and for test fluids at the reference temperature, $T_o$. Comparing the Deborah number for a given experiment to $De_{sag}$ will determine if sagging effects are important. Deborah numbers greater than $De_{sag}$ are expected to be less affected by sagging.

Gravitational sagging is a particularly important constraint in filament stretching devices if one wishes to explore experimentally the coil-stretch transition in dilute

polymer solutions at Deborah numbers of $De \approx 0.5$. For a dilute polymer solution described by the Zimm theory, the longest relaxation time may be expressed by the equation 2.10.

The critical Deborah number for sagging can thus be written in the compact form:

$$De_{sag} = \frac{\lambda_z \rho g R_o}{\eta_o} = \frac{[\eta] M_w \rho g R_o}{\zeta(3\nu) N_A k_B T (1 + [\eta]c)} \tag{5.5}$$

For the solution to be considered dilute we require $[\eta]c \leq 1$, which places an upper bound on the denominator. We know the numerical expression for the intrinsic viscosity of the typical solution that we use ([SM96a] and [SM96b]): $[\eta] = 4.2 \times 10^{-4} M_w^{0.59} dL/g$. Taking typical values of $\rho = 1026 kg/m^3$, $T_o = 298K$, $R_o = 3mm$ and requiring $De_{sag} \leq 0.5$, equation 5.5 can be reduced to:

$$1.3 \times 10^{-5} M_w^{1.59} \leq 0.5 \tag{5.6}$$

We would therefore need to use polymers with molecular weights less than $M_w \leq 765000 g/mol$ in order to explore the coil-stretch transition in the absence of appreciable gravitational sagging.

## 5.2 Preparation of the fluid

To fulfill the previous condition, we prepare a Boger fluid consisting of polystyrene and styrene oil. An adequate polystyrene is P6022-S from Polymer Source Inc. Its molecular weight is $M_w = 750000 g/mol$ and it is therefore under the limit of observation of the coil-stretch transition. $0.594g$ of polystyrene are first dissolved in toluene by mixing. The resulting solution is added to $789.52g$ of styrene oil with a density of $\rho = 1026 kg/m^3$. The higher volatility of toluene compared to styrene oil is then used to evaporate it in a vacuum oven. The characteristics of the final polymer solution called MV1 are gathered in the table 5.1.

The coil overlap concentration $c^*$ is derived from the equation 2.13.

| | **MV1** | **PS025** |
|---|---|---|
| **Density** $\rho$ $[kg.m^{-3}]$ | 1026 | 1026 |
| **Surface Tension** $\sigma$ $[N.m^{-1}]$ | 0.038 | 0.038 |
| **Concentration** $c$ $[g.L^{-1}]$ | 0.772 | 0.257 |
| **Ratio** $c/c^*$ | 0.50 | 0.273 |

Table 5.1: *Physical parameters of the polymer solution MV1 prepared to observe the coil-stretch transition, and comparison with the visco-elastic fluid PS025 defined in chapter 3.*

## 5.3 Properties of the fluid

The properties of this fluids will be determined by the same process as to find those of PS025 described in section 3.3. Then, we first concentrate on the shear rheology and later we will use extensional rheology.

### 5.3.1 Shear rheology: cone and plate rheometer

As described in section 3.3.1, the fluid MV1 is tested with a cone and plate rheometer. The properties of the cone are given in table 3.2. From steady shear flow experiments and oscillatory shear flow experiments, we can extract the dependence of viscosity with the shear rate (figure 5-1) and the storage and loss moduli fitted with the Zimm model (figure 5-2).

The zero-shear viscosity is thus found to be $\eta_0 = 53.5\ Pa.s$.

From the value of the zero-shear viscosity, the Kuhn Chain theory can be used to evaluate the solvent viscosity $\eta_s$ and the longest relaxation time $\lambda_z$ through equations 2.18 and 2.10. The results, compared to the values obtained by Zimm fitting of figure 5-2 are in table 5.2.

### 5.3.2 Extensional rheology: Caber

A series of experiments in extensional rheology has been led. As in section 3.3, the device used for these experiments is the Capillary Breakup Extensional Rheometer

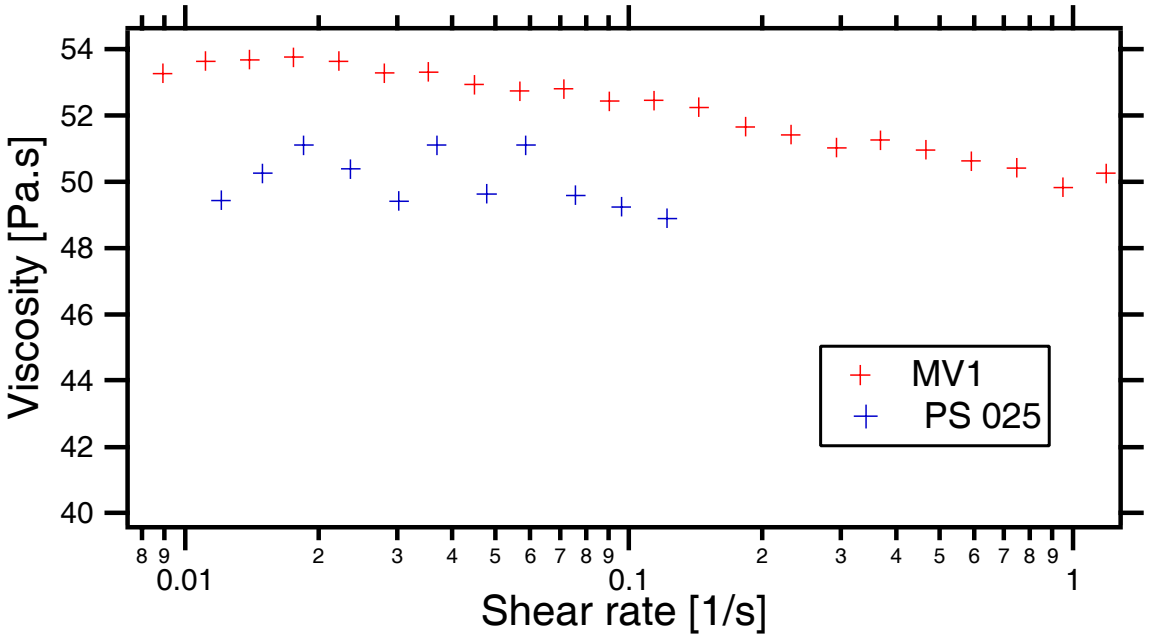


Figure 5-1: *Viscosity of the polymer solution MV1 as a function of shear rate at* $25^0C$*, and comparison with PS025.*

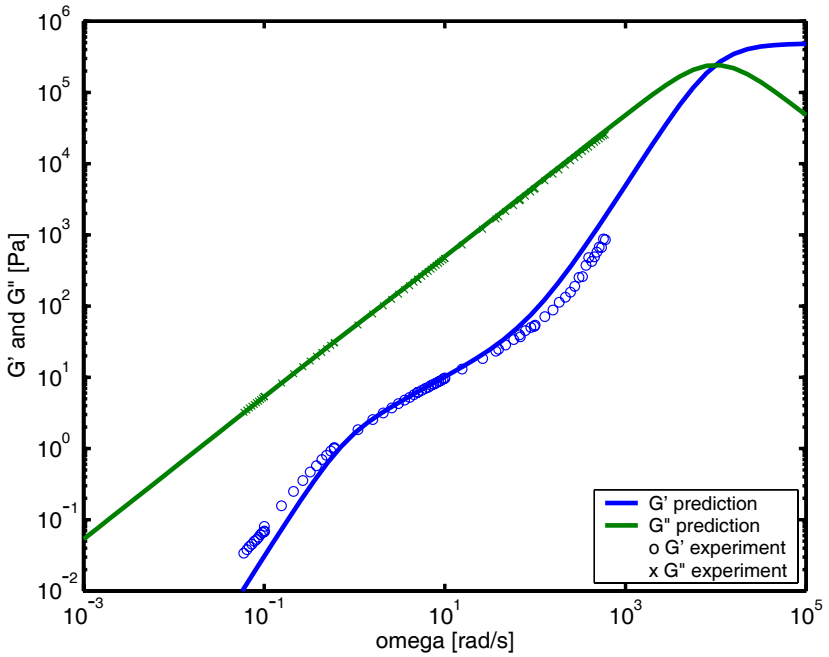


Figure 5-2: *Experimental values of storage and loss moduli fitted using Zimm theory for MV1 at* $25^0C$

| | MV1 | PS025 |
|---|---|---|
| Zero-shear viscosity $\eta_0$ $[Pa.s]$ | 53.5 | 49 |
| Solvent viscosity from Kuhn Chain $\eta_{sK}$ $[Pa.s]$ | 48.8 | 46.4 |
| Solvent viscosity from Zimm theory $\eta_{sZ}$ $[Pa.s]$ | 48.5 | 45.5 |
| Longest relaxation time from Kuhn Chain $\lambda_{zK}$ $[s]$ | 0.78 | 3.14 |
| Longest relaxation time from Zimm theory $\lambda_{zZ}$ $[s]$ | 1.04 | 5.02 |

Table 5.2: *Physical parameters of the polymer solutions MV1 and PS025 calculated from shear rheology experiments at* $25^0C$.

(Caber). The result of these experiments is shown in figure 5-3: as expected the radius of the viscoelastic solution decreases exponentially in the elasto-capillary regime (section 4.2.2). Fitting this part allows to calculate the longest relaxation time of the polymer, since the radius decreases as $e^{-t/3\lambda_z}$ (equation 4.13).

This experiment is run at the air temperature of $18.5^0C$. Therefore, the relaxation time obtained by the exponential fit has to be adjusted with the Williams-Landel-Ferry shift factor introduced in section 3.3.2 in order to know the relaxation time at the reference temperature ($25^0C$). The result is a relaxation time $\lambda_{\mathbf{zC}} = \mathbf{1.09\ s}$. Finally, the longest relaxation times determines with the Kuhn Chain model, the Zimm theory and the Caber fitting are in table 5.3.

| | **Relaxation time** $[s]$ |
|---|---|
| **Kuhn Chain model** | 0.78 |
| **Zimm theory** | 1.04 |
| **Caber fitting** | 1.09 |

Table 5.3: *Longest relaxation time of the polymer solution MV1 from three different models at* $25^0C$.

The agreement is very good between the different models. This polymer solution behaves as the visco-elastic fluid simulated in section 4.1.2. Finally, we can plot the profile of the filament during the necking thanks to the method introduced in section 3.3.4 (figure 5-4).

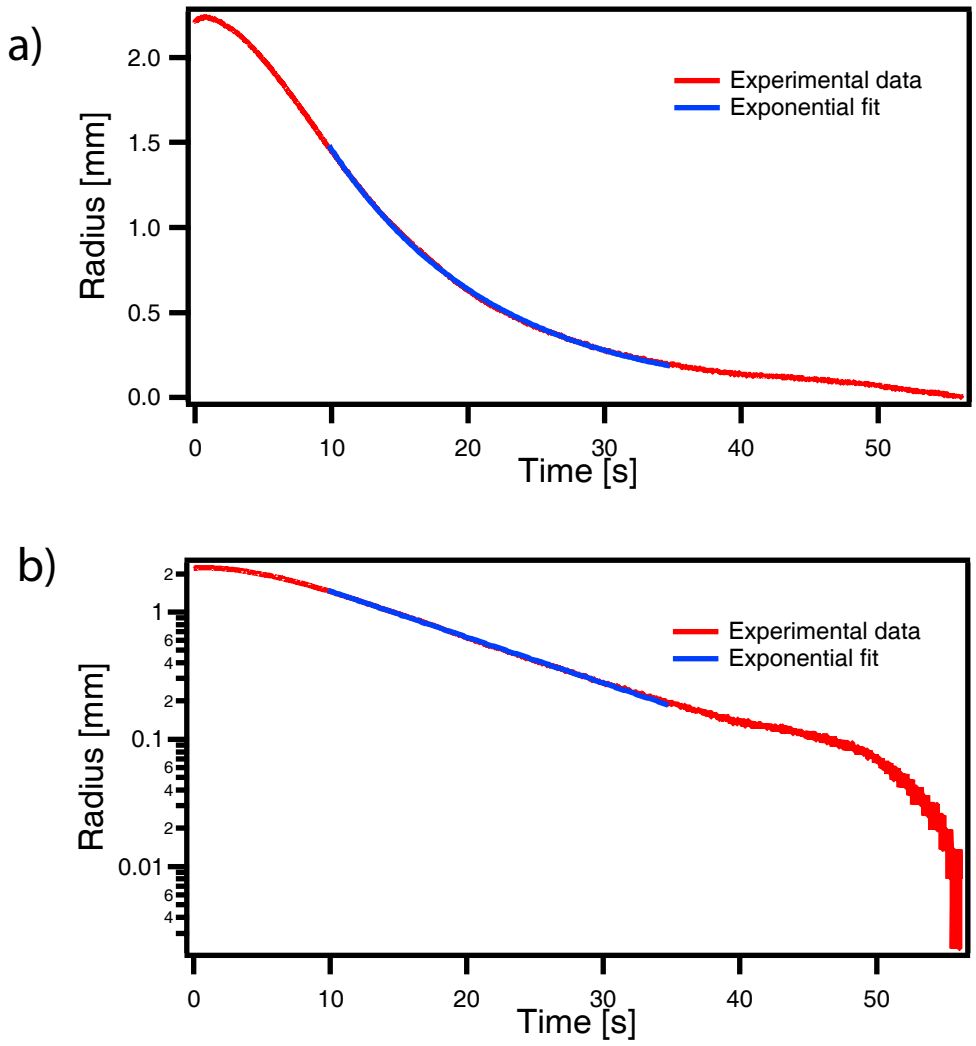


Figure 5-3: *Radius decrease during a Caber experiment and exponential fit for the polymer solution MV1 at* $T = 18.5^0C$ *on a linear scale (a) and an exponential scale (b).*

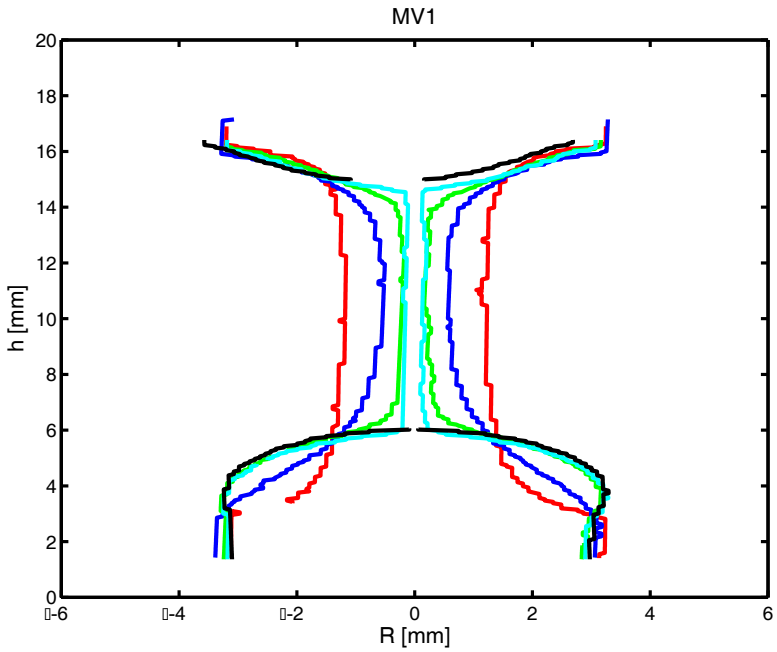


Figure 5-4: *Digitized edges of MV1 during a CABER experiment. The step of time between two successive profiles is equal to 9 seconds.*

On figure 5-4, the gravitational sagging is still visible, even if we made this fluid to be less susceptible to gravity. Nevertheless, the asymmetry between the droplet on the top plate and the droplet on the bottom plate seems less important than for PS025, as expected.

# Chapter 6

# Force transducer integration

In the numerical simulations of the Caber experiments (chapter 4), the initial axial deformation $A^0_{zz}$ remains an unknown parameter. It had be assumed to be equal to 1 for the needs of the simulation, this value corresponding to the absence of initial deformation. Nevertheless, as we will see in the following section, a way to have a direct measure of this quantity is given by measuring the force on a plate during a Caber experiment. We will then replace the bottom plate of the Caber by a Force Transducer.

## 6.1 Force on the bottom plate of a Caber

The force balance in filament stretching rheometers has been studied by Szabo and McKinley [SM03] or Bhattaccharjee et al. [BNMS03]. During a Caber experiment, the bottom plate remains stationary and the top plate accelerate upwards. It is then obvious to choose the bottom plate as arbitrary frame of reference. The force measured on the bottom plate is a normal force composed of the viscous force, the capillary force, the elastic force (in the case of a viscoelastic fluid) and the gravity. It is given by the following equation:

$$F_N = 3\eta_s\dot{\epsilon}\pi R^2(t) + \pi\sigma R(t) + \Delta\tau_p\pi R^2(t) - \rho g\pi\frac{R_0^2 L_0}{2} \tag{6.1}$$

$$= F_V + F_\sigma + F_E + F_g. \tag{6.2}$$

In this equation, $\dot{\epsilon}$ is the strain rate, $R(t)$ is the radius of the liquid filament, $\tau_p$ is the normal stress difference, $R_0$ is the initial radius of liquid (basically, it is the radius of the plate) and $L_0$ is the initial gap between the plates. This force balance is valid as well for the stretching as for the stress relaxation. The origin of time is chosen to be when the stretching is done and the two plates are held stationary. For the measure, the reference of the force is given when the sample of fluid is loaded in the Caber. So the gravity is 'tared' and is not taken into account in the experiments. In the following, the force measured on the bottom plate obeys to the equation 6.1 where the gravity has been removed.

### 6.1.1 Elongation

The top plate of the Caber goes up linearly with time. So its speed is constant $v_{plate}$ and the gap $L$ between the plates is such as: $L(t) = L_0 + v_{plate}t$. Then, according to Pearson and Connelly [PC82], the strain rate is given by:

$$\dot{\epsilon} = \frac{v_{plate}}{L} = \frac{v_{plate}/L_0}{1 + v_{plate}t/L_0}. \tag{6.3}$$

As the Caber 'opens' in 50 $ms$ between $L_0 = 3\ mm$ and $L_f = 13\ mm$, it is easy to calculate the strain rate at the end of the stretching process (at a time arbitrary chosen as $t = 0^-$). We obtain $\dot{\epsilon}_{0^-} = 15.38\ s^{-1}$. The liquid radius at the end of this process obeys to:

$$R(0^-) = R_0 e^{-\frac{3}{4}\dot{\epsilon}t} \tag{6.4}$$

$$= 1.78\ mm. \tag{6.5}$$

It is now possible to calculate the force on the bottom plate at $t = 0^-$. The contribution is the different forces at $t = 0^-$ are as follows:

$$F_V(0^-) = 2.07 \times 10^{-2}\ N \tag{6.6}$$

$$F_\sigma(0^-) = 2.12 \times 10^{-4}\ N \tag{6.7}$$

The total force measured on the bottom plate of the CABER at $t = 0^-$ is: $F_N(0^-) = 2.09 \times 10^{-2}\ N$. This corresponds to a mass greater than 2 $g$, which is out of range for the Force Transducer we use, as given in the table 6.1. So the signal measured on the bottom plate will necessarily saturate.

### 6.1.2 Stress relaxation

**Initial part:**

When the top plate stops, the filament of fluid starts necking according to the description given in chapters 3 and 4. The force measured on the bottom plate remains the force given by the equation 6.1, without the gravity term. Nevertheless, right after the stretching the radius of the liquid filament is linearly time-dependent (section 4.2) and obeys the equation:

$$R(t) = R(0^+) - \frac{\sigma t}{6\eta_s}, \tag{6.8}$$

where $R(0^+) = R(0^-)$ is the radius at the beginning of the relaxation. By definition (equation 2.4) the strain rate is:

$$\dot{\epsilon} = -\frac{2}{R}\frac{dR}{dt} \tag{6.9}$$

$$= \frac{\sigma}{3\eta_s R}. \tag{6.10}$$

At $t = 0^+$, the value of the strain rate is then: $\dot{\epsilon}_{0^+} = \frac{\sigma}{3\eta_s R(0^+)} = 0.158\ s^{-1}$. The expression of the force measured on the bottom plate is then:

$$F_N = 2\pi\sigma\left(R(0^+) - \frac{\sigma t}{6\eta_s}\right). \tag{6.11}$$

The decrease of the force is also linear with time.

**Elasto-Capillary balance:**

According to the asymptotic behaviors described in section 4.2.2, the radius of viscoelastic fluids decreases exponentially as $e^{-t/3\lambda}$. The elastic stress is $\tau_{zz} = G(fA_{zz} - 1) \approx GA_{zz} = GA^0_{zz}e^{t/3\lambda}$ and the radius is $R(t) = R_i\left(GA^0_{zz}R_i/\sigma\right)e^{-t/3\lambda}$, wihere $R_i$ is

the value of the radius at the beginning of the elasto-capillary phase. For the force measured on the bottom plate it yields:

$$F_N = F_V + F\sigma + F_E \tag{6.12}$$

with

$$F_V = \frac{2\pi\eta_s}{\lambda} R_i^2 \left(\frac{GA_{zz}^0 R_i}{\sigma}\right)^{2/3} e^{-\frac{2t}{3\lambda}}, \tag{6.13}$$

$$F_\sigma = \pi\sigma\ R_i \left(\frac{GA_{zz}^0 R_i}{\sigma}\right)^{1/3} e^{-\frac{t}{3\lambda}}, \tag{6.14}$$

$$F_E = \pi G A_{zz}^0 R_i^2 \left(\frac{GA_{zz}^0 R_i}{\sigma}\right)^{2/3} e^{-\frac{t}{3\lambda}}. \tag{6.15}$$

The visoucs force decreases faster than the elastic and the capillary force. Then, if we assume that the dynamics is given only by the elasto-capillary balance, the decrease of the force measured on the bottom plate $F_N$ is exponential. Fitting this part of the data provides an estimation of the initial stress $A_{zz}^0$ as we will see in section 6.3.2.

## 6.2 Experimental setup

### 6.2.1 General overview

The Caber has already been described in section 3.1. Its bottom plate is now replaced by a plate in Delrin plastic (McMaster-Carr Supply Company) attached to an Aurora Scientific 405A Force Transducer (figure 6-1). The radius of the plate is 3.175 *mm*. To keep the symmetry between the plates and having the same surface of contact on the top and the bottom plate, a 1 *mm*-thick plate is glued on the original top plate of the Caber (figure 6-2).

The acquisition of the data given by the laser micrometer of the Caber is done trough a National Instrument 1200 DAQ Card, as explained in section 3.1. The output of the Force Transducer System is connected to a National Instrument BNC-2110 connector block. The data is then transmitted to a computer and analyzed by the Labview routine *Analog input (ryeh mod)* written by Roger Yeh.

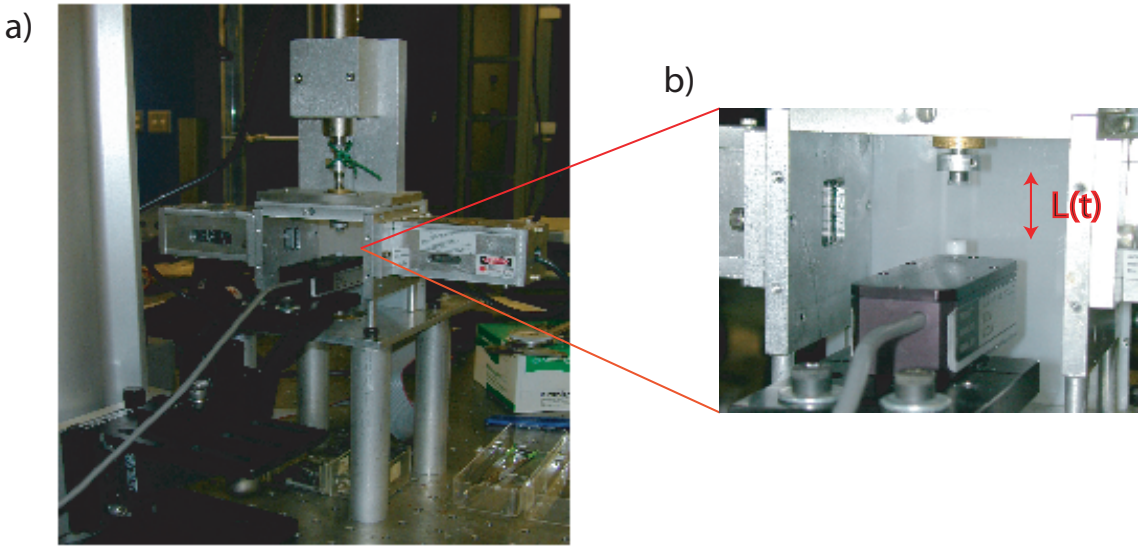


Figure 6-1: *Picture of the experimental setup for the Caber with Force Transducer.*

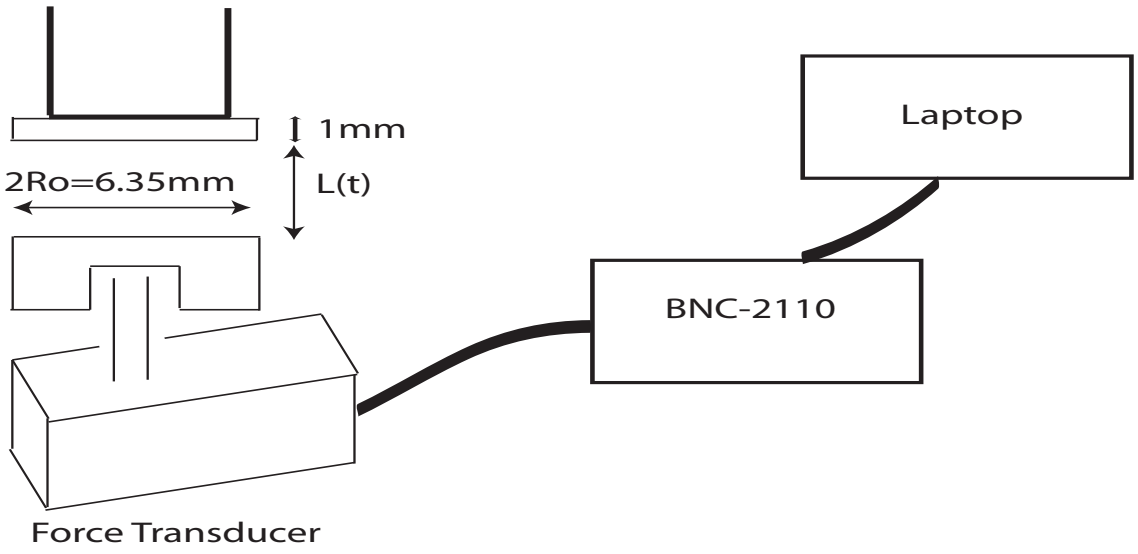


Figure 6-2: *Drawing of the experimental setup for the Caber with Force Transducer.*

### 6.2.2 Calibration

The 405A Force Transducer has a full scale of $\pm 1$ $g$. The design is based on two variable displacement capacitors formed from cantilevered, quartz beam. The load is attached to the active beam while the other beam acts as a reference. This system nullifies most ambient vibrations and electrical interference. Its output is in Volts, so it has to be calibrated to convert the output into grams. The static calibration shown in figure 6-3 consists in getting the voltage indicated for different weights varying from 20 $mg$ to 1 $g$. The experimental points have been fitted to get the slope of the response.

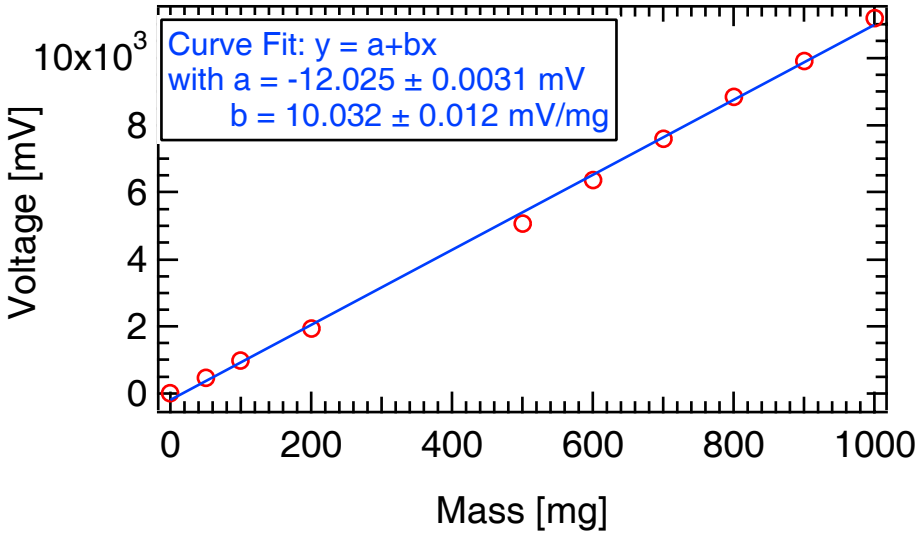


Figure 6-3: *Static calibration of the Force Transducer.*

The Force Transducer has also to be dynamically calibrated: a weight removal yields the time of response of the transducer. It has been found to be about 30 $ms$ (figure 6-4).

Because of the fact that the Caber does not present a closed area for the experiments, the Force Transducer is subject to the noise due to the draught. Then, it seems Utopian to hope having a better precision than $10^{-2}$ $V$ on a measurement. It corresponds to a precision in mass of 1 $mg$. Finally, the characteristics of the 405A

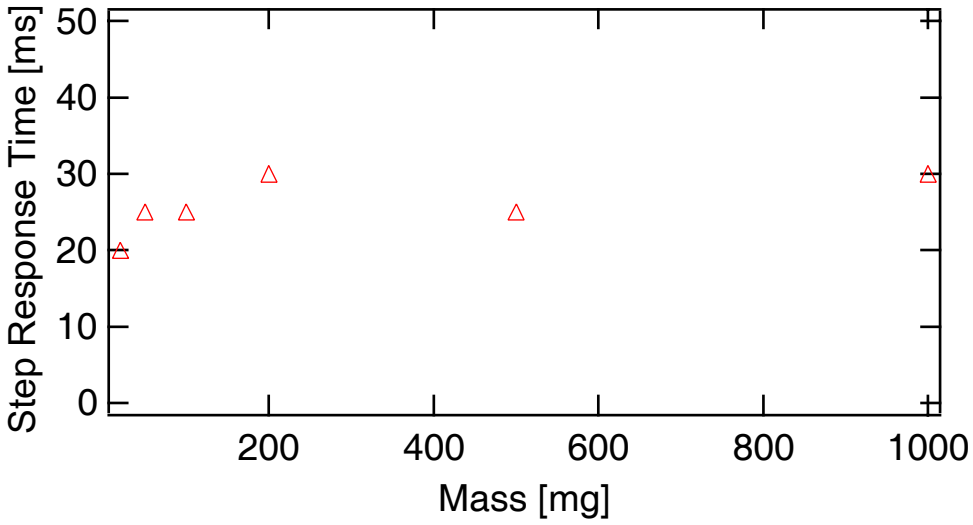


Figure 6-4: *Transient response of the Force Transducer.*

Force Transducer are gathered in table 6.1:

| **Force Transducer** | **405A** |
|---|---|
| **Range** $[\pm\, grams]$ | 1 |
| **Resolution** $[gram]$ | $10^{-3}$ |
| **Maximum overload force** $[gram]$ | 10 |
| **Sensitivity** $[volt/gram]$ | 10.032 |
| **Step Response Time** $[ms]$ | 30 |

Table 6.1: *Characteristics of the 405A Force Transducer after calibration.*

## 6.3 Results and interpretation

### 6.3.1 Experimental results

Several Caber experiments have been run with the fluids described previously in this study: styrene oil, a diluted solution of high molecular weight (PS025, section 3.2) and a solution of polystyrene with lower molecular weight (MV1, chapter 5). The results of these experiments in terms of force measured by the Force Transducer are

reported in figure 6-5. The sample rate of the data acquisition is 500 points per second.

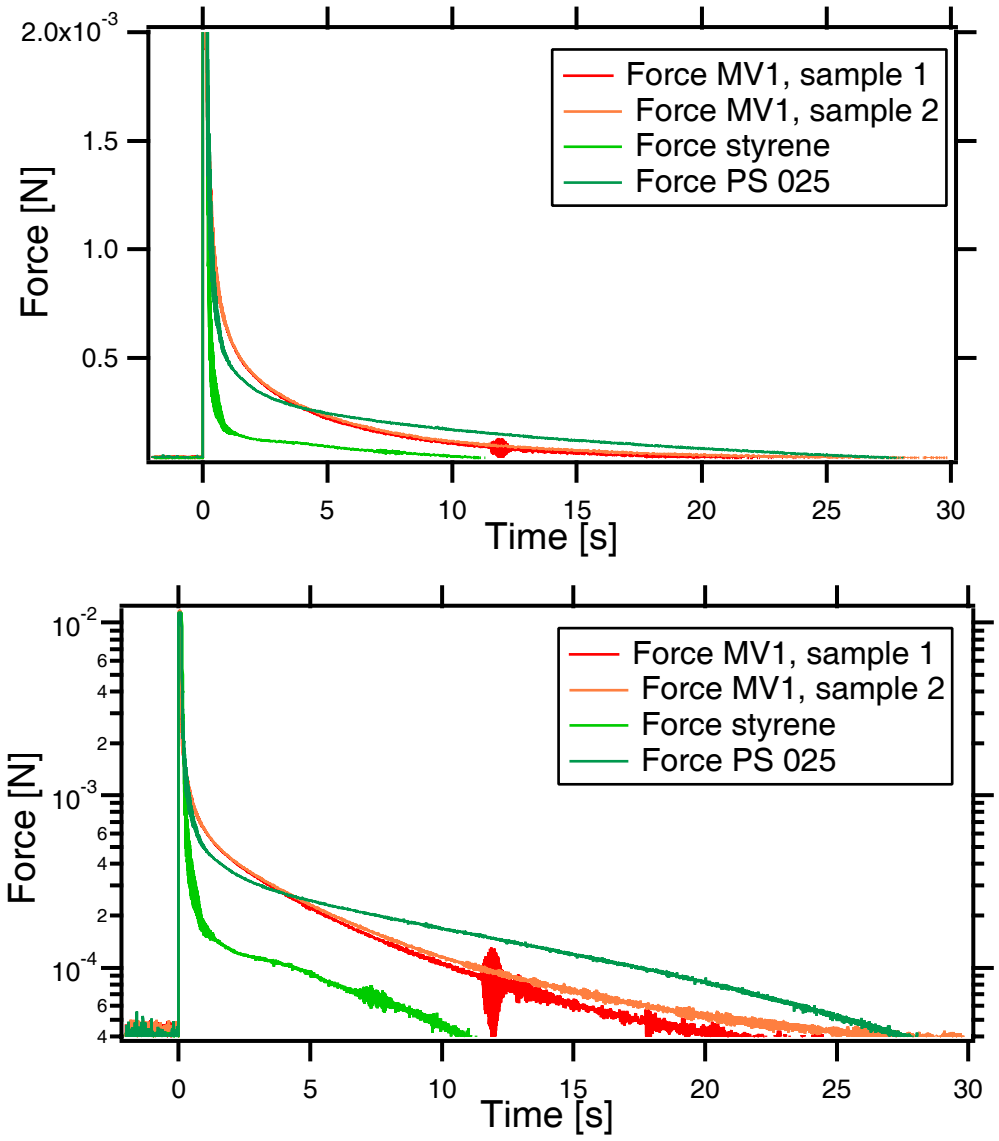


Figure 6-5: *Force on the bottom plate during a Caber experiment (linear and logarithmic scale).*

In the figure 6-5, the time $t = 0$ corresponds to the end of the stretching. The two plates are held stationary and the strain rate drops from $\dot{\epsilon}_{0-}$ to $\dot{\epsilon}_{0+}$. Then the viscous force drops and explains the fast decrease of the force just after $t = 0$. In the following part of the curve, the fluids behave as Newtonian fluids and the

radius decreases linearly, as expected (equation 6.11). The force for visco-elastic fluids (PS025 and MV1) shows an exponential time-dependence, which is clearly visible in figure 6-5 with the logarithmic scale. Neglecting the viscous force in this part, the exponential dependence can be fitted by the equations 6.14 and 6.15 to extract $A^0_{zz}$. If the exponential fit is $\alpha e^{-t/\beta}$, then $\beta = 3 \times \lambda$, where $\lambda$ is the relaxation time of the solution, and $A^0_{zz}$ is solution of the following equation:

$$\pi\sigma R_i \left(\frac{GA^0_{zz}R_i}{\sigma}\right)^{1/3} e^{-t/3\lambda} + \pi G A^0_{zz} R_i^2 \left(\frac{GA^0_{zz}R_i}{\sigma}\right)^{2/3} e^{-t/3\lambda} = \alpha e^{-t/\beta}. \qquad (6.16)$$

All the variables of this equation are given parameters, except $A^0_{zz}$ and $\lambda$, which can easily been derived.

### 6.3.2 Comparison with the model and the numerical simulation

#### Initial stress

An exponential fit of the elasto-capillary part of the force data yields a value of the initial stress $A^0_{zz}$ which is the ultimate goal of the experimental setup with the Force Transducer. It has been done on the data of the two visco-elastic fluids PS025 and MV1. The results are in the table 6.2. The slope of the exponential fit gives an estimation of the relaxation time of the polymer solutions. As this parameter has already been calculated by several methods, it represents a test of validity of the present method.

| **Fluid** | **PS025** | **MV1** |
|---|---|---|
| $\mathbf{A^0_{zz}}$ | 49.7 | 8.09 |
| **Relaxation Time** $\lambda_F$ $[s]$ | 4.83 | 1.82 |

Table 6.2: *Initial stress $A^0_{zz}$ and relaxation time obtained by exponential fit of the force measured on the bottom plate of the CABER.*

Having an estimate of the initial stress allows to run the numerical simulations

exposed in chapter 4 with a good initial condition. The Matlab code used here is *Cabersimu ultim* and its inputs are in table 6.3. We can then simulate the decrease of the force on the bottom plate of the Caber.

| Fluid | **PS025** | **MV1** |
|---|---|---|
| Density $\rho$ $[kg/m^3]$ | 1026 | 1026 |
| Surface tension $\sigma$ $[N/m]$ | 0.038 | 0.038 |
| Zero-shear viscosity $\eta_0$ $[Pa.s]$ | 49.4 | 53.5 |
| Concentration $c$ $[g/cm^3]$ | 0.0002565 | 0.000772 |
| Molecular weight $M_w$ $[kg/mol]$ | 1877 | 750 |
| Initial radius $R1$ $[m]$ | $2 \times 10^{-3}$ | $2 \times 10^{-3}$ |
| Initial axial stress $A^0_{zz}$ | 49.7 | 8.09 |

Table 6.3: *Inputs for the numerical simulation of the force measured on the bottom plate of the CABER.*

### Numerical simulations

Running the Caber-simulating code previously described in chapter 4 yields the figure 6-6.

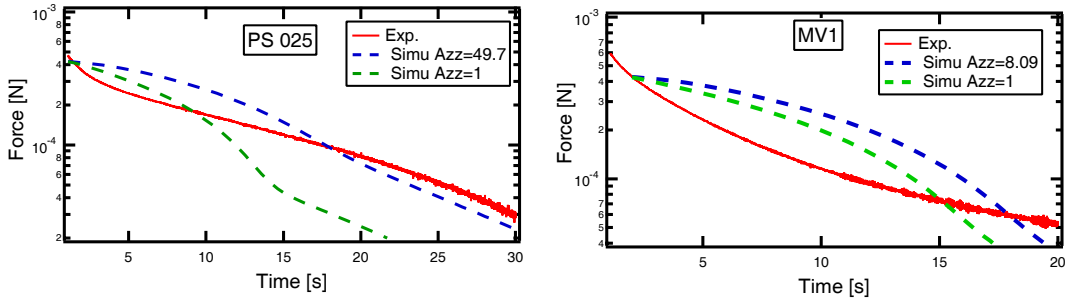


Figure 6-6: *Comparison between the force measured experimentally on the bottom plate of the Caber and the numerical simulation for the visco-elastic fluids PS025 and MV1, and for two different initial stresses* $A^0_{zz}$.

The total force measured on the bottom plate of the Caber right after the stretch-

ing (time $t = 0^+$) can be calculated from three different methods: reading the experimental data after a time $t = t_{stretching} + 2 \times t_{transient\ response} = 50\ ms + 2 \times 30\ ms$, reading the simulated curve for $t = 0$, and evaluating the equations given at the beginning of the chapter (section 6.1) at $t = 0^+$. This gives the table 6.4. The simu-

| **Fluid** | **PS025** | **MV1** |
|---|---|---|
| $\mathbf{F_{N-exp}}$ $[N]$ | $4.64 \times 10^{-4}$ | $4.49 \times 10^{-4}$ |
| $\mathbf{F_{N-num}}$ $[N]$ | $4.25 \times 10^{-4}$ | $4.26 \times 10^{-4}$ |
| $\mathbf{F_{N-an}}$ $[N]$ | $4.25 \times 10^{-4}$ | $4.25 \times 10^{-4}$ |

Table 6.4: *Initial forces on the bottom plate of a Caber: experimental, numerical and analytical values.*

lation of the decrease of the force looks quite good in the case of the fluid PS025. The improvement due to a better choice of the initial elastic stress $A^0_{zz}$ is clear. For MV1, the simulated force has the good order of magnitude but not the good behavior. It could come from an inaccuracy in the determination of $A^0_{zz}$ because the experimental data approaches the instrumental limit of $10^{-5}$ $N$.

# Chapter 7

# Conclusion and Future Work

## 7.1 Conclusion

PS025 and MV1 were the fluids studied in the current research. Simultaneously, they were compared to the Newtonian solvent of these solutions: the styrene oil. The experimental study of PS025 and its derivatives in chapter 3 proved a dependence of the relaxation time of the solution with the concentration of the fluid, even for very diluted polymer solutions. This scaling is a new step in the study of polymer solutions and it is at variance with the classic models such as the Kuhn Chain, which predict a non-dependence with concentration (equation 2.10). Thanks to numerical simulations based on a single mode FENE-P model (chapter 4), we were able to break down the necking of a visco-elastic filament during a CABER experiment into three successive asymptotic behaviors: a visco-capillary part, an elasto-capillary part and finally a fully extended limit. Then, we established a criterion on the molecular weight of the polymer $M_w$ through a characteristic time scale $\delta = \frac{\lambda}{\eta_s R_0/\sigma}$ to observe the Non-Newtonian behavior of a Boger fluid (section 4.3.2). We also made another visco-elastic fluid, called MV1, with a polymer of smaller molecular weight. As explained in section 5.1, it aimed at testing a fluid less susceptible to gravity. Indeed, even if we did not consider the gravity in the dynamics of fluids such as PS025, we know from observation, and edge recognition methods (section 3.3.4), that the filament of liquid is subject to gravitational sagging. Profiles of the new fluid MV1 such as figure

5-4 proved its weaker dependence with gravity. Finally, in the previous numerical simulations, the initial axial stress $A^0_{zz}$ was an unknown that we had to guess. It was then fixed at 1, even if we already knew that this value was wrong. Integrating a force transducer to the CABER allowed to measure directly $A^0_{zz}$, and then to use a better value. It clearly improves the correspondence of experimental data and numerical simulation, as shown in figure 6-6. A graphical summary of the current research in the case of the visco-elastic fluids PS025 and MV1 is exposed in figures 7-1 and 7-2.

## 7.2 Future Work

### 7.2.1 Technical issues

The experimental setup CABER + Force Transducer is not optimal. The incompatibility between the DAQCard-1200 data acquisition card and the BNC-2110 connector board explains why we had to use two different computer for the CABER and the Force Transducer. This raises the problem of the synchronization of the two signals. This would be better to use directly the CABER software for the force data with the free channel already devoted to the Force Transducer in the CABER software. It would also be very useful to have a CABER with a controlled temperature. It would reduce the number of experimental data we need to fit, and it would avoid the use of shift factors such as the Williams-Landel-Ferry shift factor (section 3.3.2).

### 7.2.2 Simulation issues

An improvement for the simulation would be to use a multi-mode FENE-P and not a single mode FENE-P model as done in the current research. The Matlab code used for the CABER simulations offers already the possibility of working with several modes. Thus, the numerical simulations of the force decrease and of the evolution of the force during CABER experiments would maybe fit better with the experimental data. At the beginning of the necking, the difference in the shape between experimental data and numerical simulation (as can be seen in figure 7-1) may be solved in the case of

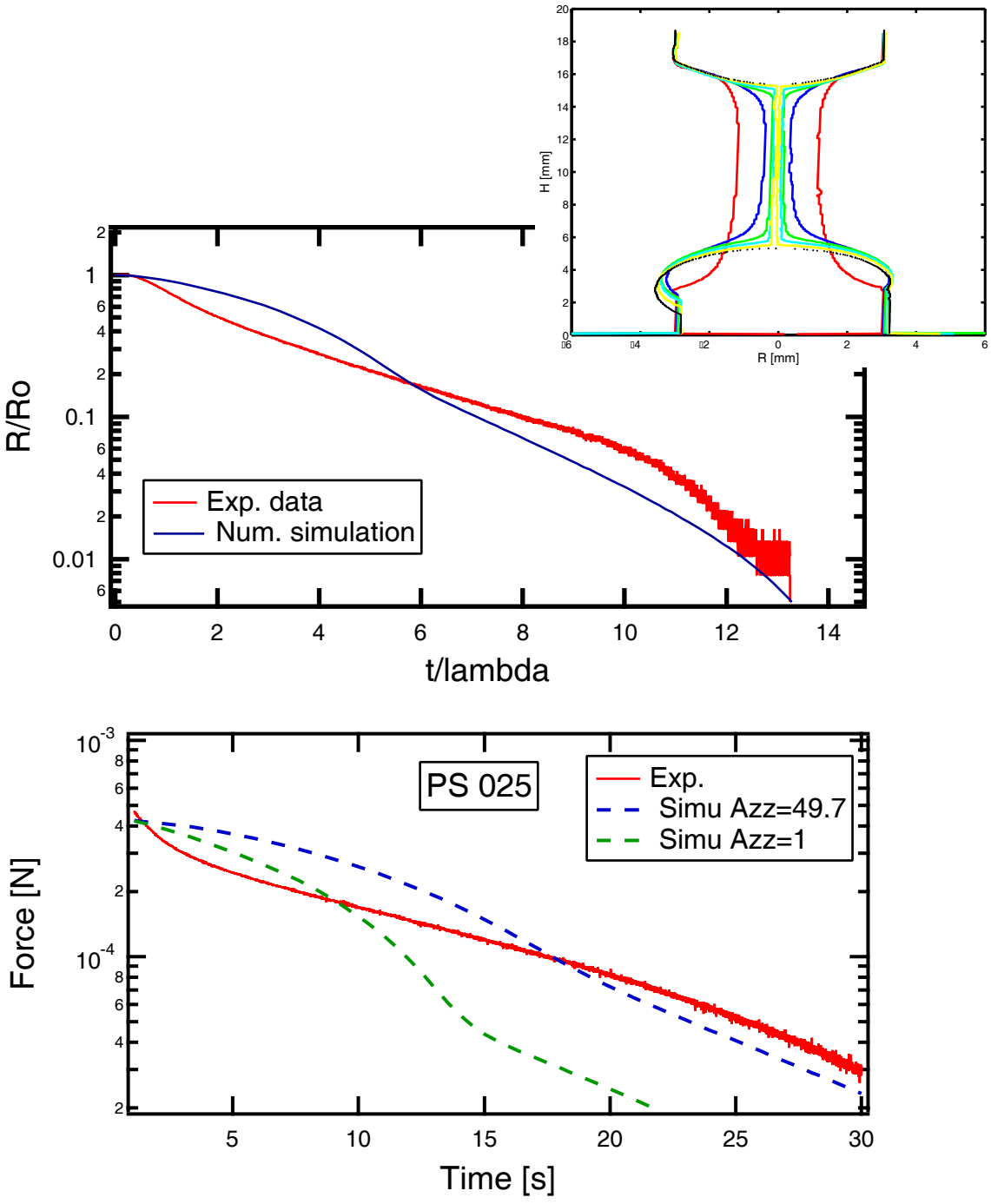


Figure 7-1: *Experimental data and simulation of the evolution of the radius and the force during a CABER experiment for PS025. On the step strain imposed the initial gap and the final gap betwwen the plates are respectively* $L_0 = 3\ mm$ *and* $L_f = 14\ mm$.

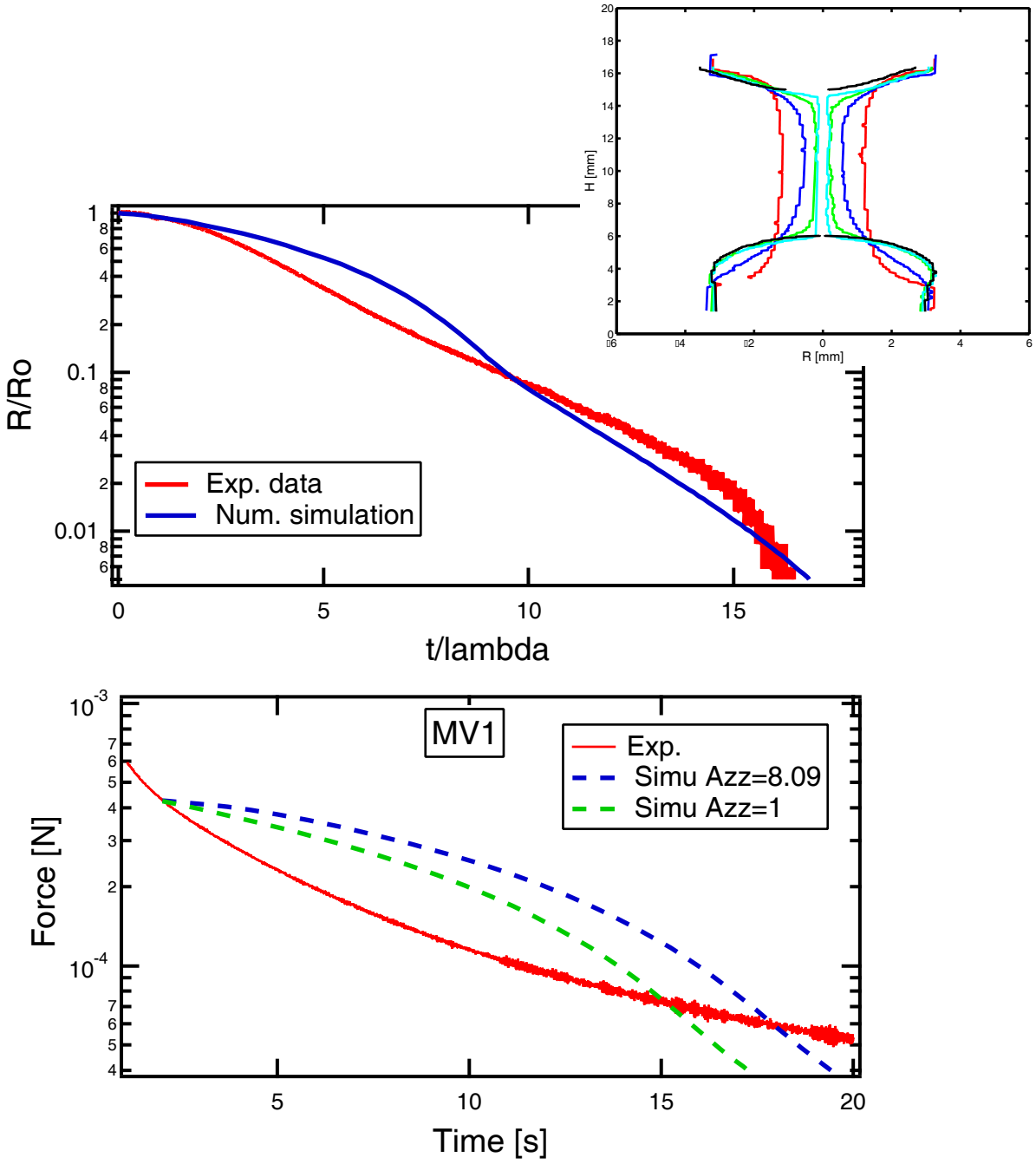


Figure 7-2: *Experimental data and simulation of the evolution of the radius and the force during a CABER experiment for MV1. On the step strain imposed the initial gap and the final gap betwwen the plates are respectively* $L_0 = 3\ mm$ *and* $L_f = 14\ mm$.

a multi-mode model.

According to the the FENE-P model based on one-dimensional analysis by Entov and Hinch, the logarithmic plot of the force versus the radius during a CABER experiment should be linear: the force monotonically decays towards zero at the same necking rate as the filament radius. A simulation of the forces obeying to Giesekus and FENE models has been recently performed by Fontelos and Li [FL04]. Nevertheless, no experimental study has ever demonstrated this behavior. The figure 7-3 is then the first to present experimental data of this kind. The main part of the curves presented for the viscoelastic fluids PS025 and MV1, and the Newtonian solvent (Styrene Oil) are linear. As expected, this clearly shows that the force and the radius decay at the same rate. This is not the case right after the stretching, as the viscous force drops due to the the sudden drop of the strain rate (section 6.1). The data here is limited by the minimum force we can measure with our experimental setup: as indicated in section 6.2.2, the minimum force we can measure is $F = 10^{-5}\ N$. The minimum radius that we can measure ($R = 20\ \mu m$) is not constraining here. Clearly, there is an issue with MV1. It could come from the fact that the fluid drains during the necking process. Then, the gravitational force which had been "tared" in the force balance is too small to balance the real contribution of the gravity. It would explain why the force keeps being constant when the radius decreases. In the figure 7-4, this residual gravity has been removed from the force data of MV1, and the plot corresponds to what we expected.

This field presents interesting features for a future work.

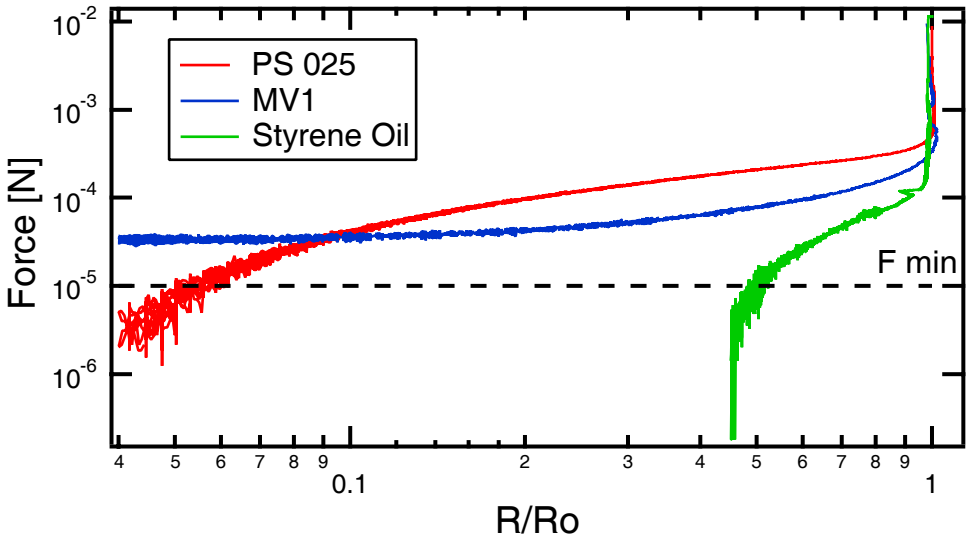


Figure 7-3: *Plot in log-log scale of the force measured on the bottom plate of the CABER as a function of the radius of the liquid filament.*

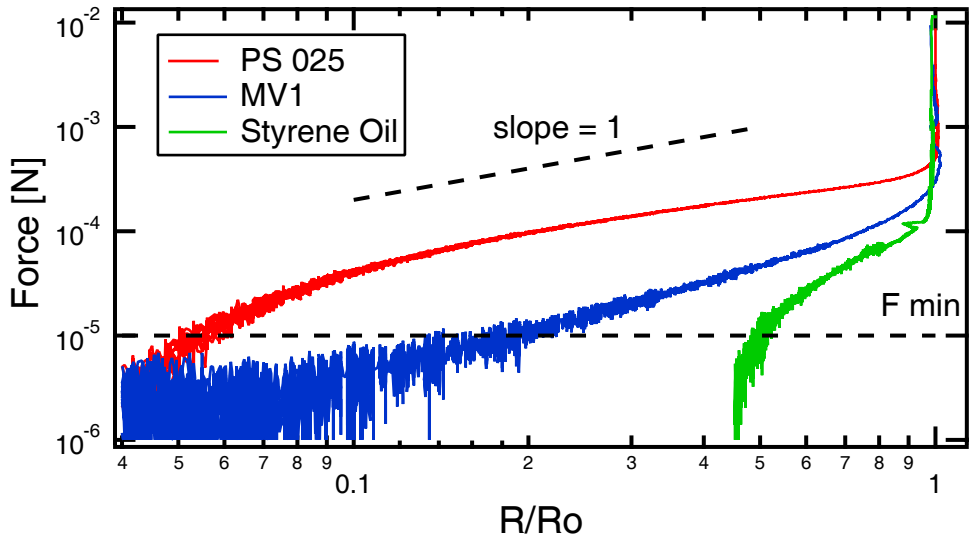


Figure 7-4: *Plot in log-log scale of the force measured on the bottom plate of the CABER as a function of the radius of the liquid filament. The residual contribution of the gravity for MV1 has been removed.*

# Bibliography


[AM01] S.L. Anna and G.H. McKinley. Elasto-capillary thinning and breakup of model elastic liquids. *Journal of Rheology*, 45:115–138, jan-feb 2001.

[AMN+01] Shelley L. Anna, Gareth H. McKinley, Duc A. Nguyen, Tam Sridhar, Susan J. Muller, Jin Huang, and F. David James. An interlaboratory comparison of measurements from filament-stretching rheometers using common test fluids. *Journal of Rheology*, 45:83–114, jan-feb 2001.

[Ann00] Shelley L. Anna. *Filament Stretching of Model Elastic Liquids*. Doctor of philosophy, Harvard University, Engineering and Applied Sciences, 2000.

[BAH87] R. Byron Bird, Robert C. Armstrong, and Ole Hassager. *Dynamics of Polymeric Liquids: Fluid Mechanics*, volume 1. John Wiley & Sons, New York, 1987.

[BAHC87] R. Byron Bird, Robert C. Armstrong, Ole Hassager, and Charles F. Curtiss. *Dynamics of Polymeric Liquids: Kinetic Theory*, volume 2. John Wiley & Sons, New York, 1987.

[BARH03] Anders Bach, Kristoffer Almdal, Henrik Koblitz Rasmussen, and Ole Hassager. Elongational viscosity of narrow molar mass distribution polystyrene. 2003.

[BER01] A. V. Bazilevsky, V. M. Entov, and A. N. Rozhkov. Breakup of an oldroyd liquid bridge as a method for testing the rheological properties of polymer solutions. *Polymer Sciences*, 43:716–726, 2001.

[BNMS03] P. K. Bhattacharjee, D. A. Nguyen, G. H. McKinley, and T. Sridhar. Extensional stress growth and stress relaxation in entangled polymer solutions. *Journal of Rheology*, 47:269–290, 2003.

[dG97] P.G. de Gennes. Molecular individualism. *Science*, 276:1999–2000, 1997.

[DSMS98] P. S. Doyle, E. S. G. Shaqfeh, G. H. McKinley, and S. H. Spiegelberg. Relaxation of dilute polymer solutions following extensional flow. *Journal of Non-Newtonian Fluid Mechanics*, 76:79–110, 1998.

[Egg93] Jens Eggers. Universal pinching of 3d axisymmetric free-surface flow. *Physical Review Letters*, 71:3458–3460, 1993.

[Egg97] Jens Eggers. Nonlinear dynamics and breakup of free-surface flows. *Reviews of Modern Physics*, 69:865–929, 1997.

[EH97] V. M. Entov and E. J. Hinch. Effect of a spectrum of relaxation times on the capillary thinning of a filament of elastic liquid. *Journal of Non-Newtonian Fluid Mechanics*, 72:31–53, 1997.

[Ent99] V. M. Entov. Polymer solutions elongational flow: suspension of extensible rods model. *Journal of Non-Newtonian Fluid Mechanics*, 82:167–188, 1999.

[Fer80] J. D. Ferry. *Viscoelatic Properties of Polymers*. Wiley, New York, third edition, 1980.

[FL04] Marco A. Fontelos and Jie Li. On the evolution and rupture of filaments in giesekus and fene models. *Journal of Non-Newtonian Fluid Mechanics*, "in press", 2004.

[Gra80] Wiliam W. Graessley. Polymer chain dimensions and the dependence of viscoelastic properties on concentration, molecular weight and solvent power. *Journal of Rheology*, 21:258–262, 1980.

[HLL03] Chih-Chen Hsieh, Lei Li, and Ronald G. Larson. Modeling hydrodynamic interaction in brownian dynamics: Simulations of extensional flows of dilute solutions of dna and polystyrene. *Journal of Non-Newtonian Fluid Mechanics*, 113:147–191, 2003.

[Keu97] R. Keunings. On the peterlin approximation for finitely extensible dumbbells. *Journal of Non-Newtonian Fluid Mechanics*, 68:85–100, 1997.

[KS99] M. I. Kolte and P. Szabo. Capillary thinning of polymeric filaments. *Journal of Rheology*, 43:609–625, 1999.

[Lar88] Ronald G. Larson. *Constitutive Equations for Polymer Melts and Solutions*. Butterworths, 1988.

[LM94] R.F. Liang and M.R. Mackley. Rheological characterisation of the time and strain dependence of polyisobutylene solution. *Journal of Non-Newtonian Fluid Mechanics*, 52:387–405, 1994.

[Mac94] C. W. Macosko. *Rheology: Principles, Measurement and Applications*. Wiley-VCH, New York, 1994.

[MS02] Gareth H. McKinley and Tamarapu Sridhar. Filament-stretching rheometry of complex fluids. *Annual Review of Fluid Mechanics*, 34:375–415, 2002.

[MT00] G. H. McKinley and A. Tripathi. How to extract the newtonian viscosity from capillary breakup measurements in a filament rheometer. *Journal of Rheology*, 44:653–670, 2000.

[Pap95] D. T. Papageorgiou. On the breakup of viscous liquid threads. *Physics of Fluids*, 7:1529–1544, 1995.

[Par03] Anna E. Park. Extensional viscosity of complex fluids and the effects of pre-shear. Master's thesis, MIT, Department of Mechanical Engineering, 2003.

[PC82] G. H. Pearson and R. W. Connelly. The use of extensional rheometry to establish operating parameters for stretching processes. *Journal of Applied Polymer Science*, 27:969–981, 1982.

[Pip86] A. C. Pipkin. *Lectures on viscoelasticity theory*. Springer-Verlag, New York, second edition, 1986.

[Rei69] M. Reiner. The deborah number. *Physics Today*, 17:62, 1969.

[Ren94] M. Renardy. Some comments on the surface-tension driven break-up (or the lack of it) of viscoelastic jets. *Journal of Non-Newtonian Fluid Mechanics*, 51:97–107, 1994.

[Ren95] M. Renardy. A numerical study of the asymptotic evolution and breakup of newtonian and viscoelastic jets. *Journal of Non-Newtonian Fluid Mechanics*, 59:267–282, 1995.

[RH99] H. K. Rasmussen and O. Hassager. Three-dimensional simulations of viscoelastic instability in polymeric filaments. *Journal of Non-Newtonian Fluid Mechanics*, 82:189–202, 1999.

[Rhe96] *Rheolyst Series AR1000 Rheometer: Hardware Manual*. TA Instruments, 1996.

[Rou53] P. E. Rouse. A theory of the linear viscoelastic properties of dilute solutions of coiling polymers. *Journal of Chemical Physics*, 21:1272–1280, 1953.

[SM96a] M. J. Solomon and S. J. Muller. Study of mixed solvent quality in a polystyrene-dioctyl phtalate-polystyrene system. *Journal of Polymer Science: Part B: Polymer Physics*, 34:182–192, 1996.

[SM96b] M. J. Solomon and S. J. Muller. The transient extensional behavior of polystyrene-based boger fluids of varying solvent quality and molecular weight. *Journal of Rheology*, 40:837–856, sept-oct 1996.

[SM03] Peter Szabo and Gareth H. McKinley. Filament stretching rheometer: Inertia compensation revisited. *Rheologica Acta*, 42:269–272, 2003.

[Tan99] Roger I. Tanner. *Engineering Rheology*, volume 52. Oxford University Press, second edition, 1999.

[Ten95] *Digital Tensiometer K 10 ST User Manual*. Kruss USA, 1995.

[WLF55] M. L. Williams, R. F. Landel, and J. D. Ferry. The temperature dependence of relaxation mechanisms in amorphous polymers and other glass-forming liquids. *Journal of the American Chemical Society*, 77:3701–3707, 1955.

[Zim56] B. H. Zimm. Dynamics of polymer molecules in dilute solution: Viscoelasticity, flow, birefringence and dielectric loss. *Journal of Chemical Physics*, 24:269–280, 1956.